Ordered mesoporous "one-pot" synthesized Ni-Mg(Ca)-Al2O3 as effective and remarkably stable catalysts for combined steam and dry reforming of methane (CSDRM)

Karam Jabbour, Pascale Massiani, Anne Davidson, Sandra Casale, Nissrine El Hassan

Ordered mesoporous "one-pot" synthesized Ni-Mg(Ca)-Al$_2$O$_3$ as effective and remarkably stable catalysts for combined steam and dry reforming of methane (CSDRM)

Karam Jabbour,[a,b] Pascale Massiani,[a,c]* Anne Davidson,[a] Sandra Casale,[a] Nissrine El Hassan[b]**

[a] Sorbonne Universités, UPMC Université Paris 06, Laboratoire de Réactivité de Surface, 4 place Jussieu, 75005 Paris, France

[b] Department of Chemical Engineering, Faculty of Engineering, University of Balamand, P.O. Box 33, Amioun, El Koura, Lebanon

[c] CNRS UMR 7197, UPMC, Laboratoire de Réactivité de Surface, 4 place Jussieu, 75005 Paris, France

Corresponding Authors:

*: Pascale Massiani, CNRS UMR 7197, UPMC, Laboratoire de Réactivité de Surface, 4 place Jussieu, 75005 Paris, France. pascale.massiani@upmc.fr

**: Nissrine El Hassan, Department of Chemical Engineering, Faculty of Engineering, University of Balamand, POBox 33, Amioun, El Koura, Lebanon.
nissrine.hassan@balamand.edu.lb

ABSTRACT

Two series of $Ni_{x\%}$ (x: 5-10 wt%) and $Ni_{5\%}M_{5\%}$ (M: Ca or Mg) containing mesoporous Al_2O_3 catalysts were prepared by "one-pot" synthesis following an evaporation-induced self-assembly (EISA) method. After reduction, the catalysts showed very high Ni dispersion within the structured oxide matrix giving high activities and long-term stabilities in combined steam and dry reforming of methane (CSDRM) carried out at 800 °C. Both the increase of Ni content and the addition of Mg (or Ca) are beneficial to performances, with activity levels reaching the maximum-expected thermodynamic ones for $Ni_{10\%}Al_2O_3$. In the Mg (or Ca) free catalysts, a relationship between nickel content, reactivity level and carbon deposition is found. Nevertheless, carbon formation is not detrimental to catalytic stability due to predominant formation of carbon nanotubes outside the nickel containing alumina grains. Addition of Ca or Mg suppresses to a great extent carbon deposition and leads to high selectivity towards the targeted CSDRM reaction, with almost no occurrence of side reactions. The remarkable thermal stability of the ordered-mesoporous alumina structure (along 40 h of run) along with the stabilization of well-dispersed Ni^0 within the alumina matrix are shown to be key factors accounting for the excellent long term catalytic performances in spite of the harsh conditions (temperature and steam) imposed by the reaction

1. INTRODUCTION

The excessive emission of large quantities of CO_2 (important anthropogenic greenhouse gas) upon industrial combustion of fossil fuels (natural gas, coal and oil) and its uncontrollable impact on global warming represent nowadays a worldwide concern [1]. While it is essential to reduce greenhouse gases, it is also of strong interest to find routes to transform them into valuable products. At present, a relevant technology resides in the transformation of carbon dioxide to molecules having industrial added values. Amongst such technologies, great attention is focused on the production of synthesis gas (syngas, gaseous mixture of CO and H_2) that constitutes a versatile building block for subsequent production of synthetic fuels or chemical intermediates in petrochemical industries [2]. Particularly, combined steam and dry reforming of methane (CSDRM, $3CH_4 + 1CO_2 + 2H_2O \rightarrow 8H_2 + 4CO$), also known as bireforming [3-6], appears as a very promising CO_2 valorization route yielding a syngas with H_2/CO molar ratio close to 2, called metgas [3-6]. The latter can be directly used in methanol [4-10] or dimethylether production [5-10] as well as in some Fisher-Tropsch operations aiming the preparation of long hydrocarbons chains [11,12]. By comparison, conventional dry reforming of methane (DRM, $CH_4 + CO_2 \rightarrow 2H_2 + 2CO$) and steam reforming of methane (SRM, $CH_4 + H_2O \rightarrow 3H_2 + CO$) yield a H_2/CO ratio of either 1 (too low) or around 3 (too high), respectively, which imposes supplementary stages (often expensive) if adjustment of the product ratio near 2 is required for the next steps of the process [3-6,13,14]. Moreover, from a sustainable point of view, the CSDRM reaction presents as additional benefit to consume CH_4, CO_2 and water as main reactants, these gases being also those present in biogas, a non-fossil fuel resource [3-6]. Thus, CSDRM offers a way to produce metgas from renewable energy sources without the need of auxiliary separation and purification procedures.

Compared to SRM and DRM, bibliographic reports on CSDRM are less numerous due to the highest complexity of this reaction that requires steam and high temperatures, as already discussed in our recent paper [15]. The main direction for catalyst development in this field is focused on the use of nickel as active phase, this transition metal being the most attractive candidate for large-scale industrial applications due to its high reactivity in DRM and SRM [3-5] together with low cost and wide availability compared to noble metals (Ru, Rh, Ir) [16-19]. However, the stability of supported Ni-based catalysts under the harsh reaction conditions of CSDRM [20-23] is still an important concern. The major deactivation drawbacks are severe coke deposition, reoxidation and thermal agglomeration of the Ni^0 nanoparticles under steam and at high temperature [24-39].

For SRM and DRM catalysts, it was recently found that confinement of the nickel active phase within structured pores of oxide supports, especially mesoporous silica [40-42] or alumina [43-46], helps minimizing Ni^0 sintering during reaction, thus preserving reactivity with time on stream. Another effective approach to limit nanoparticles growth consists in forming a solid solution between impregnated nickel and the support by using appropriate synthesis techniques [3-5,24,25]. This is expected to stabilize the active phase by enhancing metal-support interaction (MSI) but also to limit coke formation associated to nickel sintering. Based on these approaches, we recently developed a mesoporous Ni-containing alumina catalyst obtained by combining 1) active phase introduction directly during the synthesis ("one-pot" synthesis allowing solid solution formation) and 2) use of an evaporation-induced self-assembly (EISA) method [47,48] in presence of a structuring agent (to obtain a mesoporous material). The resulting catalyst, with nickel nanoparticles highly dispersed and stabilized inside the structured alumina matrix, was found significantly more active and stable in long term CSDRM operation than impregnated catalysts [15].

Another general way to overcome deactivation relies on the introduction of secondary elements giving basic and/or redox properties to the catalyst. Table 1 summarizes available data dealing with this approach for CSDRM. Considering alumina-based materials with impregnated nickel, the most tested catalysts in this reaction, the presence of MgO [26,37,39], mixed CeO_2-ZrO_2 [38] or CeO_2 [28,34] was shown to inhibit deactivation whereas severe activity loss were seen in the absence of such added elements, with conversion levels dropping down by more than 50%, in some cases, after less than 20 h of reaction (Table 1). Similarly, mixed MgO-Al_2O_3 oxides derived from hydrotalcite like-materials were described as suitable supports leading to high CSDRM catalytic performances [37], even if some studies reported some deactivation on such type of systems and a need to add auxiliary elements to maintain stable performances [32,34-36]. Besides, catalysts with alumina-magnesia core-shells structures as supports were reported promising, demonstrating however a lack of selectivity towards metgas production [31]. It is commonly accepted that basic modifiers (e.g. MgO) in the catalyst formulation promotes CO_2 adsorption/activation on the surface and its subsequent reaction with neighbour carbon $C_{(s)}$ deposits, leading globally to CO production ($CO_2 + C_{(s)} \rightarrow 2CO$) [26,30,37]. Likewise, the addition of active oxygen carriers such as CeO_2 and/or ZrO_2 within Ni-based catalysts (Table 1) is known to result in oxidative removal of $C_{(s)}$ deposits via their combustion with surface oxygen giving CO_2 [32,34,35]. However, most of the reported tactics that involve addition of a secondary element over

"standard" commercial oxides require several successive time-consuming post-synthesis treatments, particularly i) a step of high temperature calcination of the support prior to its utilization to generate mixed oxides (as in hydrotalcite like-materials [24,32-37] and in some cases in alumina [26-29,37]), ii) subsequent calcination after Ni and/or co-element impregnation [3-5,24-26,28-30,32-39] and iii) eventually high temperature steam treatment (H_2/H_2O) following a H_2 reduction session [25].

Based on this state of the art, the present work aimed at combining the special advantages for CSDRM of (i) one-pot synthesized mesoporous nickel alumina catalysts with (ii) the promising behaviour expected by addition of a basic modifier. It is worth noting that, even if the benefits of ordered mesoporous oxide supports (particularly silica) is now well established for methane reforming reactions as was reviewed recently [49], the positive impact of structured mesoporous supports other than silica has not yet been established for CSDRM, except in our recent preliminary paper [15]. Thus, the goal was to develop "one-pot" mesoporous nickel alumina based catalysts containing a basic modifier for effective combined steam and dry reforming operation. As far as we know, such approach combining (i) structuration of the porous alumina support and (ii) active phase - and supplementary element - insertion within the catalyst matrix by "one-pot" synthesis was not yet considered for the CSDRM reaction (Table 1). Low cost and widely available Mg^{2+} and Ca^{2+} containing salts were chosen as additives based on their potentiality to yield basic properties (in their oxide form) and on their known positive impact on CSDRM (Table 1) and DRM [50-52]. For the sake of completion, the influences of the Ni content (5-10 wt% range) and of the nature and amount of the identified carbon species on the activity level and long-term stability were also considered.

2. EXPERIMENTAL PROCEDURES

2.1. Synthesis of mesoporous "one-pot" alumina based-materials

The mesoporous $Ni_{x\%}Al_2O_3$ (with x = 5, 7.5 or 10 wt %) and $Ni_{5\%}M_{5\%}Al_2O_3$ (where M = Mg or Ca) samples were synthesized following a procedure inspired (with some modifications) from the known "one-pot" evaporation-induced self-assembly (EISA) method [47-48]. For each synthesis, approximately 1.0 g of P123 Pluronic triblock copolymer $((EO)_{20}(PO)_{70}(EO)_{20}$, $M_n=$ 5800, Sigma Aldrich, 43546-5) was dissolved at room temperature (RT) in 20 ml of absolute ethanol (CH_3CH_2OH, Sigma Aldrich, 64-17-5) under vigorous stirring. Then, 1.6 ml nitric acid

(65.0 wt% aqueous HNO_3, Johnson Matthey S.A., extra pure) was added, still under stirring, together with A mmol of aluminium isopropoxide ($Al(OPr^i)_3$, $C_9H_{21}AlO_3$, 98+%, Sigma Aldrich, 220418), B mmol of nickel nitrate hexahydrate ($Ni(NO_3)_2.6H_2O$, Sigma Aldrich, 13478-007) and eventually C mmol of either magnesium nitrate hexahydrate or calcium nitrate tetrahydrate ($Mg(NO_3)_2 \cdot 6H_2O$ or $Ca(NO_3)_2.4H_2O$, Sigma Aldrich 13446-18-9 and 13477-34-4, respectively). All employed chemicals were used as received, without further purification. The total molar composition was always kept constant, equal to 10 mmol (i.e. [A + B] = 10 mmol for $Ni_{x\%}Al_2O_3$ samples and [A + B + C] = 10 mmol for $Ni_{5\%}M_{5\%}Al_2O_3$ ones). The resulting mixture was covered with a polyethylene (PE) film, continuously stirred at RT for at least 7 h until complete dissolution and finally transferred into a beaker placed for 48 h in a digital auto-regulator water-bath (Stuart SWB6D) set at 60 °C to undergo slow evaporation (ethanol, acid). The obtained green xerogels, which color deepened with increasing Ni content (in line with increasing octahedral Ni^{2+} ions amounts), were calcined slowly in air at 600 °C for 5 h (heating rate 0.5 °C.min^{-1}) to give calcined "one-pot" synthesized alumina-based materials.

2.2. Characterization techniques

Textural properties were determined from N_2-sorption (adsorption and desorption) isotherms recorded on an ASAP 2020 Micromeritics apparatus. Prior to experiments, the samples were degassed under vacuum for 3 h at 300 °C then cooled down back to room temperature before being placed at liquid nitrogen temperature for measurements. Single point pore volumes were determined from the adsorption isotherms at a relative pressure of 0.990. Brunauer-Emmett-Teller (BET) surface areas were calculated from BET equation for a relative pressure (P/P$_0$) range between 0.05 and 0.25. Pore size distributions were calculated using the Barrett-Joyner-Halenda (BJH) method applied to the adsorption branch of the isotherm. For spent catalysts, calcination in air at 450 °C/5 h (0.5 °C.min^{-1}) was performed prior to N_2-sorption analysis to remove carbon deposits before analysis.

Structural properties were studied by powder X-ray Diffraction (XRD) at small and wide angles. The small-angle measurements were done from 2θ of 0.5 ° to 4.0 ° (time per step: 1 s) on a BRUKER type D8 ADVANCE diffractometer equipped with a Cu Kα irradiation source (λ = 1.5418 nm) and operating at 40 kV and 30 mA. The wide-angles data were obtained on a PANalytical XPert^3 diffractometer using a Cu Kα radiation (λ= 1.5405 nm), a voltage of 30 kV, a current of 10 mA and a step size of 0.04 ° (with 2s duration at each step). The acquisitions were done

in a 2θ range from 20.0 to 90.0 °. Crystalline phase identification was based on comparison with standard powder XRD files published by the international center for diffraction data (ICDD). Coherent domain sizes were calculated using the Scherrer's equation: $D_{(hkl)} = (K\lambda/\beta cos\Theta)$, where $K=$ 0.9 is the shape factor for spherical particles, λ is the X-ray wavelength, β is the full width at half maximum (FWHM) of the diffraction peak and Θ is the peak position.

The reducibility of the Ni-alumina based materials was studied by temperature-programmed reduction (H_2-TPR) on an Autochem 2920 unit, Micromeritics. The calcined powder (100 mg) was loaded in a U-shaped quartz reactor and heated from RT up to 900 °C at a constant rate of 7 °C.min^{-1} under a 5 vol% H_2/Ar flow (30 ml.min^{-1}). The overall H_2 consumption was constantly recorded by thermal conductivity detection (TCD). Before arrival to the detector, the gas flow was passed through a cold trap (composed of ice and NaCl) in order to condense any water generated during the experiment (NiO + $H_2 \rightarrow Ni^0 + H_2O$). This ensures that the detected signal (difference in thermal conductivity between reference and analysis gases) is fully related to H_2 consumption with no interference of formed water.

Transmission electron microscopy (TEM) observations were done on ultrathin sections of solids to correctly visualise the dispersed nickel nanoparticles (and eventual coke deposits) and their location inside or outside the porous alumina grains. The sections were prepared as follows: a few milligrams of powder were mixed with an EPON 812 embedding resin in a beam capsule. Polymerization of the mixture took place at 60 °C for 48 h, then the polymerized blocks were cut with a diamond knife in slices (50-70 nm in thickness) that were deposited on copper grids covered with a carbon membrane layer. TEM images were taken on a JEOL-JEM 200 electron microscope operating at 200 keV (LaB$_6$ gun). Average metallic Ni^0 particle sizes were estimated using the "Comptage de Particules" LRS software considering at least 500 particles present in grains with main elongation axis (channels) orientated parallel to the electronic beam (i.e. pore openings perpendicular to the beam). Scanning electron microscopy (SEM) micrographs were registered on a Hitachi SU-70 SEM-FEG microscope with an electron acceleration tension of 7 kV.

TGA/DSC were performed on a TA SDT Q600 thermal analyzer instrument from RT to 900 °C (heating rate of 10 °C.min^{-1}) in flowing air (50 ml.min^{-1}). Raman spectra were collected on a KAISER (RXN1) optical system equipped with a charge-coupled detector (CCD), a laser with λ = 785 nm (energy of 1.58 eV) and a microscope with an X50 long working distance (W.D. = 8.0

mm) lens. The operation conditions were as follows: 10 mW laser power, 4 cm^{-1} resolution, 10s acquisition time and a total of 30 accumulations per spectrum.

2.3. Thermodynamic simulation of the CSDRM reaction

Simulations were performed using the HSC 7.1 Chemistry software (where H, S and C stand for the enthalpy, entropy and heat capacity, respectively) which principle is to calculate, based on the Gibbs free energy minimization's principle [53], the equilibrium gas composition depending on the applied conditions (initial molar gas mixture, temperature, pressure, etc.). For reasons detailed in section 3.3, the chosen initial gaseous $CH_{4(g)}/CO_{2(g)}/H_2O_{(g)}/Ar_{(g)}$ composition was 1/0.4/0.8/12 (Ar is used as inert diluent). $C_{(s)}$ (carbon in solid phase) was introduced as possible product (initial composition set at zero). Equilibrium compositions (unconverted reactants and expected $H_{2(g)}$, $CO_{(g)}$ and $C_{(s)}$) products) were determined in the 100-1000 °C temperature range.

2.4. Reactivity measurements

Catalytic tests were conducted at atmospheric pressure (P= 1 atm) in a Microactivity (PID Eng and Tech) vertical fixed-bed continuous flow stainless steel (SS310) reactor (9 mm internal diameter). Prior to reaction, the calcined powder was *in-situ* reduced at 800°C/3h under a flow (30 ml.min^{-1}) of 5 vol % H_2/Ar in order to ensure complete nickel reduction, then the flow was switched to the reactant mixture ($CH_4/CO_2/H_2O/Ar$=1/0.4/0.8/12). Water was introduced by a syringe pump (Teledyne ISCO, D-series, model 5000) in the form of liquid water (0.005 ml.min^{-1}), evaporated (6.15 ml.min^{-1}) at 180 °C (hotbox temperature) and mixed with the other gases before feeding the reactor. The total gas hourly space velocity (GHSV) was 69 L.g$_{cat}$$^{-1}$.hr^{-1} or 138 L.g$_{cat}$$^{-1}$.hr^{-1} (using 100 and 50 mg catalyst weight, respectively). The reaction temperature was controlled by a thermocouple placed in the middle of the catalyst bed. The effect of temperature (600-800 °C range) on CH_4 and CO_2 conversions upon either increase or decrease of the temperature was evaluated along successive 3h stabilization steps at each temperature. Long-term stability measurements were carried out at 800 °C for 40 h.

Before analysis, the effluent was passed through a gas/liquid separator to condense the residual steam present in the exhaust gas after reaction. Next, the reactants and products were quantified by on-line gas chromatography using a Micro-GC Inficon equipped with a thermal conductivity detector (TCD) and two columns placed in parallel for the detection of CH_4, H_2 and CO (Molecular Sieve column)

and of CO_2 (plot U column). The results will be hereafter expressed as conversion of CH_4 (XCH_4), conversion of CO_2 (XCO_2), and H_2/CO ratio calculated according to Eqs. (1)-(3):

$$XCH_4(\%) = \frac{[CH_4]_{in} - [CH_4]_{out}}{[CH_4]_{in}} \times 100 \tag{1}$$

$$XCO_2(\%) = \frac{[CO_2]_{in} - [CO_2]_{out}}{[CO_2]_{in}} \times 100 \tag{2}$$

$$\frac{H_2}{CO} = \frac{mol\ of\ H_2\ produced}{mol\ of\ CO\ produced} \tag{3}$$

3. RESULTS AND DISCUSION

3.1 Textural and structural properties of calcined samples

The textural and structural properties of calcined materials were analysed by N_2 sorption and by small and wide angles XRD measurements. The N_2 sorption isotherms (Figure 1A) are of type IV for all samples, with H_1-shaped hysteresis loops and steep capillary condensation steps at P/P_0 = 0.6-0.8 typical of ordered mesoporous structures with parallel and cylindrical channels [47,54]. The desorption branch for $Ni_{5\%}Al_2O_3$ (curve b, Figure 1A) is slightly different than for other samples, with a shape characteristic of "ink-bottle" interconnected pores having different size distributions of cavities and necks [55]. This could be due to some experimental uncertainty during preparation of this sample that was the first synthesized according to our experimental procedure (not yet optimized). In spite of such small difference, the well-ordered 2D hexagonal structure (p6mm symmetry) is also attested in all synthesised materials by the low angle X-ray diffraction patterns (Figure 1B) that show two peaks at circa 0.94° and 1.5° (even if very weak for the second for the doped materials), characteristic of the [100] and [110] plane reflections, respectively [47].

The good textural properties of all samples can also been seen from the values of surface area, pore volumes and pore diameters deduced from the isotherms (Table 2). Particularly, in all the $Ni_xAl_2O_3$ series, the surface areas are in the range 200-225 $m^2.g^{-1}$, as high as in previous reports on mesoporous alumina synthesized under comparable conditions [47]. For all samples (except $Ni_{5\%}Al_2O_3$ with "poorly-controlled" texture), the pores sizes distributions are quite sharp

(diameter between 8 and 12 nm), within the conventional range for mesoporous materials. At higher Ni content, the adsorption branch of the hysteresis loop gradually shifts to higher relative pressures, revealing larger pores, and the phenomenon is slightly accentuated for the Mg and Ca containing samples. Again, this trend is in accordance with the shifts towards lower angles seen in the small angles XRD patterns (Figure 1B). This increase could be related to the nitrate ions added in the medium during synthesis (present as counter ions in the Ni, Mg and Ca precursors), which could acidify the ethanol solution with subsequent enlargement of pore diameters as was already proposed [54]. Such pH effect, together with possible access restriction to some pores by occluded species, could also contribute to the slight loss of surface area and pore volume seen in $Ni_{5\%}Al_2O_3$ compared to Ni-free Al_2O_3, and accentuated in $Ni_{5\%}Mg_{5\%}Al_2O_3$ and $Ni_{5\%}Ca_{5\%}Al_2O_3$. It is worth recalling here that such textural changes cannot derive from the activation procedure since all samples underwent the exact same thermal treatments. Besides, the main notable evolution in the $Ni_{x\%}Al_2O_3$ series is the increase of pore volume with Ni enrichment, as already reported on analogous "one-pot" synthesized Ni-alumina materials calcined at 400 °C, but not yet clarified [47].

With respect to high angles XRD measurements, all calcined materials exhibit a comparable pattern (Figure 1C), independently on the Ni (and eventually Mg or Ca) content. Thus, only weak broad diffraction peaks characteristic of a γ-Al_2O_3 phase (ICDD file # 10-0425) with small crystalline domains are observed, and no peak attributable to nickel crystalline phases is seen in the Ni loaded samples, revealing an amorphous character or an extremely high dispersion of the nickel species (if indeed present, as expected, in the materials).

Confirmation that nickel-based species were present in all Ni-enriched materials was obtained from TPR profiles of calcined nickel loaded samples that all showed a main reduction peak at rather high temperature (550-800 °C, curves b-f, Figure 2A). Such type of profile, already reported for "one-pot" synthesized Ni-alumina materials [44], is typical of the reduction of oxidized Ni strongly interacting with the support, as in spinel mixed phases characterized by strong MSI [56]. Remarkably, no peak of weakly bounded Ni species (reduction temperature below 500°C) such as those identified on non-porous impregnated alumina samples [15,43,56] was detected, revealing strong support metal interaction for all introduced nickel. For both $Ni_{5\%}Mg_{5\%}Al_2O_3$ and $Ni_{5\%}Ca_{5\%}Al_2O_3$ materials, a peak at very high temperature (above 800 °C) is also seen (profiles e and f, Figure 2A), although very weak, possibly indicative of Ni in even stronger interaction and/or of some reduction of Mg or Ca derived species. As expected, no

reduction peak was detected over pure alumina (profile a, Figure 2A). Experimental H_2-uptakes (200-900 °C range) estimated from above profiles are compared in Table 2 to theoretical uptakes calculated by (i) considering the expected Ni content in each nickel-loaded sample and (ii) assuming a bivalent nickel oxidation state after calcination. The excellent agreement between values is also attested by the linear correlation between H_2-uptakes and Ni contents (Figure 2B). This proportionality confirms that all nickel introduced in the solution during synthesis (i) is recovered in the solid after preparation, (ii) is present at a divalent state in the calcined materials and (iii) is fully reducible below 900 °C. Combined with the close peak positions for all samples, this stresses out the similar nature of the Ni species, independently of the material composition. Moreover, it is worth recalling that these species were not detected in X-ray diffraction patterns (section 3.1), revealing an amorphous state and/or a high dispersion of nickel oxide nanospecies having crystalline domains with sizes below the XRD detection limit. Small shifts in the position of the main peak are nevertheless noted between samples. In the $Ni_{x\%}Al_2O_3$ series (profiles b-d, Figure 2A), the temperature of the maximum of the peak increases from 626 °C to 631 °C then 645 °C when passing from 5 to 7.5 then 10 wt% Ni. Recalling that TPR is carried out in dynamic conditions, such trend could simply result from the different nickel contents, higher amounts of reducible species shifting the maximum of the process towards higher temperatures. Differences in Ni-based particles sizes could also play a role, but this is not probable here in view of the close Ni dispersion in all samples discussed below (section 3.7). Contrarily, for both $Ni_{5\%}Mg_{5\%}Al_2O_3$ and $Ni_{5\%}Ca_{5\%}Al_2O_3$ samples, the peak slightly shifts towards lower temperatures (peak maxima around 610 °C, profiles e-f, Figure 2A) compared to $Ni_{5\%}Al_2O_3$ with same Ni content (peak maximum around 630 °C, profile b, Figure 2A), suggesting some weakening of the nickel-support interaction when Mg or Ca are present. A similar observation was previously attributed to a potential competition between nickel and calcium/magnesium in the interaction with the alumina substrate [57]. Also, an effect of the overall acido-basic properties with changes of the chemical composition could be involved.

The textural features of the samples were also examined after reduction (800 °C, 3h). Compared to their calcined forms, the reduced materials showed slightly smaller specific surface areas and reduced pore volumes (Table 2) indicative of some thermal contraction of the alumina framework and/or pore surface condensation by dehydration and/or dehydroxylation during the

high temperature reduction treatment [58]. The values remain however fully satisfying for mesoporous materials treated at such temperature, revealing a high thermal resistance.

3.3 Thermodynamics aspects and choice of catalytic conditions

Before CSDRM testing, the best conditions to use for conducting the reaction were checked from thermodynamic simulations. Equilibrium values at atmospheric pressure (as used in the experiments) were thus determined for the applied gaseous composition, taking into account possible formation of a carbon solid phase (representing carbon deposition that cannot be ignored during practical reforming conditions). From the obtained gases concentrations plotted as a function of temperature between 100 and 1000 °C (Figure 3A), CSDRM can be viewed as a multi-reactions network where various reactions occur simultaneously, at levels that depend on the operating temperature. The possible reactions (i.e. main CSDRM that combines SRM and DRM, and side reactions [59]) as well as their favourable temperature zones are specified in Table 3.

Both steam and dry methane reforming (and therefore CSDRM as well) predominantly take place above 600 °C but with co-existence of some side reactions until 750 °C (particularly methane decomposition, WGS and RWGS, Table 3). This yields, in the 600-750 °C temperature range (Figure 3B), to H_2:CO molar products ratios far above the desired value of about 2, and to "apparent" very low CO_2 conversions that illustrate the high occurrence of water gas shift reaction producing CO_2, the latter being then not only a reactant but also a product of reaction. Effective combination of both SRM and DRM (i.e. CSDRM) to produce metgas is therefore not possible unless operating above 750 °C (upper zone 3 and zone 4 in Table 3).

Besides, although the $C_{(s)}$ profile shows significant decrease of carbon formation above 750 °C (Figure 3A), CH_4 decomposition still remains one possible reaction route at such high temperatures. This can ultimately cause severe catalytic deactivation in case of graphitic carbon deposition (even in low amount) as often observed with Ni-based methane reforming catalysts (including CSDRM ones, Table 1). A recognized solution to overcome this drawback while keeping a good control of the final product ratio close to 2 consists in adding some excess H_2O and CO_2 in the gas feed ($CH_4/CO_2/H_2O$=1/0.4/0.8 instead of 1/0.33/0.66 theoretically expected for pure CSDRM) [3,4,26,28,37]. This composition and a temperature of 800 °C were consequently selected as operating conditions, being consistent with those currently applied for CSDRM (Table

1). For the sake of completion, the effect of temperature on activity levels was also analysed through measurements carried out between 600 and 800 °C upon either temperature increase or decrease.

3.4 Catalytic performances of alumina-based catalysts

Prior to catalytic runs, the calcined mesoporous materials were *in-situ* reduced till 800 °C to generate the Ni^0 metal state active in methane reforming. The flow was then switched to that of reactants (GHSV of 138 $L.g_{cat}^{-1}.h^{-1}$) and the catalytic measurements were performed upon stepwise temperature decrease down to 600 °C. The obtained conversion values (XCH_4, XCO_2) and product ratios (H_2:CO) are listed in Table 4 and plotted as a function of temperature in Figure 4 (where the X-axis scale follows the decreasing temperature order applied during the experiments).

As expected from the endothermic character of the CSDRM reaction, both CH_4 and CO_2 conversions declined with temperature decrease and the effect was more pronounced for CO_2, particularly at temperatures below 700 °C (Figure 4B). This is in accordance with the interference of WGS side-reaction discussed above (section 3.3). As also anticipated, an amelioration of the CH_4 and CO_2 conversions (curves a-c, Figures 4A,B) was seen upon increase of the Ni content from 5 to 10 wt%, till reaching activity levels close to the maximum ones imposed by thermodynamics (dashed-lines).

More interestingly, addition of 5 wt% Mg (or Ca) was beneficial to both CH_4 and CO_2 conversions (curves d and e, Figures 4A,B) compared to the catalyst with same 5 wt% Ni content but without additive (curve a, Figures 4A,B), and the reactivity then even exceeded that of $Ni_{7.5\%}Al_2O_3$ (curve b, Figures 4A,B) in spite of a lower nickel content. The reason of such enhanced activity in presence of either Mg or Ca, already reported in the literature [60-62], will be discussed in section 3.8.

Complementary experiments involving again temperature variations were done by decreasing the temperature down to 600 °C after the *in-situ* H_2-activation step (carried at 800 °C as above), then switching the gaseous feed to flowing reactants and conducting the measurements upon stepwise heating up to 800°C (in place of stepwise decrease as done before). The thus obtained new activity levels led to a classification of catalysts as above ($Ni_{10\%}Al_2O_3$ > $Ni_{5\%}Mg_{5\%}Al_2O_3$ > $Ni_{5\%}Ca_{5\%}Al_2O_3$ > $Ni_{7.5\%}Al_2O_3$ > $Ni_{5\%}Al_2O_3$) but the conversions at a given temperature were systematically lower in the second set of experiments (Table 4). Moreover, at each temperature, the recorded H_2:CO molar ratio significantly deviated from the expected thermodynamic value,

suggesting higher occurrence of side reactions. Both phenomena, indicative of lower catalytic performances, demonstrate that starting the catalytic run under stream at 800 °C (in place of 600 °C) is a more efficient stabilization procedure. A reason of the lowest reactivity attained after starting the catalysts testing at 600 °C could be the enhanced $C_{(s)}$ deposition (Figure 3A) occurring at this temperature (Table 3), leading to irreversible poisoning and/or access restriction to some active sites that become less numerous even upon subsequent heating at higher temperatures.

3.5 Long-term catalytic stability and selectivity to metgas

Long-term stability tests, a critical issue for catalyst development, were carried out at 800 °C for 40 h under reactant stream, directly after *in-situ* H_2-reduction (best conditions, as discussed above). The space velocity was kept at 138 $L.g_{cat}^{-1}.h^{-1}$ (as above) because such condition were found appropriate for operating the reaction far enough from thermodynamic limitations at 800°C (see Figures 4A,B), which is indeed requested to allow comparisons of activity levels between catalysts. On the contrary, the experiments carried out at a lower space velocity (69 $L.g_{cat}^{-1}.h^{-1}$) led to conversions only few % below thermodynamic equilibrium (Table 5), due to the high performances of the present samples, being therefore hardly exploitable for comparisons purpose.

For all catalysts, the CH_4 conversions (Figures 5A,A'), CO_2 conversions (Figures 5B,B') and H_2:CO molar ratios (Figures 5C,C') were found extremely stable with time-on-stream. In the $Ni_{x\%}Al_2O_3$ series, the reactivity order was as above (Figures 5A,B), following the Ni content order even if being not proportional to it. This may indicate diffusional limitations or, most probably, a number of active sites not proportional to the metal amount, suggesting in turn either a higher accessibility hindrance to the active Ni^0 nanoparticles with nickel enrichment or a decrease of metal dispersion.

With respect to Mg and Ca additives, their beneficial effect towards conversions is still observed, even if less pronounced with Ca than with Mg (Figure 5A',B'). Owing to the stable activity levels, it can also be seen that the CO_2 conversion is slightly lower than that of CH_4, on both catalysts, in accordance with the excess CO_2 in the gas feed (see section 3.3) and with the thermodynamic values that estimate the CO_2 conversion lower by almost 6% than that of CH_4 at 800°C (Figure 3B). Moreover, the H_2:CO molar ratio obtained on these materials is close to 2 all along the 40 h of test (Figure 5C'), demonstrating the absence (or very limited occurrence) of side reactions on these catalysts. By contrast, the H_2:CO molar ratio progressively deviates away

from 2 with Ni enrichment in the $Ni_{x\%}Al_2O_3$ series (Figure 5C and Table 5) and the CH_4 conversion simultaneously approaches that of CO_2 (Table 5). In view of the H_2:CO ratio significantly above 2 for the two Ni-richest samples, methane cracking that can occur at 800°C and that produces $C_{(s)}$ and H_2 (Table 3) appears as the most probable side reaction taking place on these catalysts. This reaction consumes CH_4 and takes place over metal Ni^0 nanoparticles where it can produce carbon deposits, possibly blocking the active sites and lowering methane conversion [14]. The reason why CO_2 is not simultaneously affected could be linked to the high surface area of the alumina based-catalysts containing slightly basic sites where CO_2 adsorption (then activation) could continue. For the sake of completion, it has to be recalled that RWGS that consumes CO_2 and produces CO is also possible at high temperature (Table 3), but its occurrence seems less probable since it would lead to a decrease (rather than increase) of the H_2:CO ratio.

Therefore, in addition to high activity levels, especially when doped with Mg or Ca additive, our "one-pot" synthesized mesoporous catalysts show excellent catalytic stabilities along high temperature CSDRM operation, at least as high or even better than those described in the few existing reports on CSDRM alumina-based catalysts (Table 1). By comparison, addition of MgO (5-20 wt%) on impregnated Ni/Al_2O_3 [26] or mesoporous Ni/SBA-15-based samples [39] was found beneficial when conducting the same reaction at 750 °C- 850 °C but the amelioration was limited. Also, high and stable CH_4 and CO_2 conversions were reported over core-shells $Ni@Al_2O_3$ and $Ni@MgO-Al_2O_3$ catalysts, but the selectivity to metgas was low (H_2:CO ratio as high as 2.70), even on the hydrotalcite like MgO containing sample, in spite of conditions favorable to its production [31]. Besides, CSDRM performances as good as ours were attained on impregnated $Ni_{7.5\%}/Al_2O_3$ [25] and $Ni_{12\%}/MgO-Al_2O_3$ [24] catalysts featuring solid solution characteristics, but the preparation routes were quite complex with successive energy consuming (high temperature) and time-consuming (several steps) pre- and post-synthesis catalyst treatments.

3.6 Quantity and nature of coke after long term high temperature catalytic testing

To further understand the reasons of the good CDSRM performances of our samples, the spent catalysts (after stability run at 800 °C/40 h) were characterized by several techniques able to inform on coke deposits and on nickel dispersion and location. Combined TGA and DSC was carried out in flowing air, between 300 °C and 900 °C, to quantify carbon contents in the spent materials and identify the type of involved $C_{(s)}$ species from the temperatures at which they are

oxidized (particularly sp^2 (grapheme, nanotubes) and sp^3 (graphite) carbon types) [63,64]. For all spent catalysts, the TGA profiles consisted of a main weight loss over a large temperature range (Figure 6A, Table 5), fully attributable to carbon removal (as checked by on line mass spectrometry), and the DSC profiles showed three distinct peaks (Figure 6B).

The first remarkable information provided by these data is the drastic decrease of the overall $C_{(s)}$ contents (Table 5) when comparing the spent $Ni_{x\%}Al_2O_3$ catalysts (between 9 and 19 wt% carbon) and the spent Mg-or Ca- modified ones (below 4 wt% carbon). This is in accordance with the above-mentioned methane decomposition occurring as side reaction on the former samples but not on the latters (section 3.5). Secondly, in the spent $Ni_{x\%}Al_2O_3$ series, the coke content increases with Ni content, and it consequently follows activity levels as well. This is better illustrated on Figure 7 that shows on a same graph the levels of methane conversions (average values from stability tests) and the coke contents for all catalysts. Such a correlation was in fact predictable since samples with more numerous active sites (higher Ni content) converting a higher quantity of reactants (higher conversions) should produce more carbon-based species (higher C content). Nevertheless, this trend no longer stands with the $Ni_{5\%}Mg_{5\%}Al_2O_3$ and $Ni_{5\%}Ca_{5\%}Al_2O_3$ catalysts that generate high reactivity levels but very low carbon amounts (Figure 7), stressing again the peculiarly high resistance to coking of the Mg (or Ca) enriched materials. It can be also added that to stability tests performed on the $Ni_{x\%}Al_2O_3$ series of catalysts at 69 $L.g_{cat}^{-1}.h^{-1}$ in place of 138 $L.g_{cat}^{-1}.h^{-1}$, produced less coking (Table 5) contrarily to what can be expected from higher contact time and related higher conversion levels (Table 5). Nevertheless, in such experimental conditions, the activity levels approached thermodynamic limits, due to the high reactivity of the samples, and it can then be assumed that only part of the active sites participate to the catalytic act, which may reduce the contribution of side reactions compared to the main one (many active sites remaining available).

Coming back to the DSC profiles (Figure 6B), the three distinct exothermic peaks reveal co-existence of at least three types of coke-derived species, currently described as (i) weakly stable amorphous Cα (sp^2 C-atoms, superficial C or graphene-like species, peak 300-450 °C), (ii) Cβ (C-nanotubes, peak 450-550 ˚C) and (iii) stable crystalline Cγ graphite (sp^3 C-atoms, peak above 550 °C) [63]. From the predominant high temperature signal seen for all spent $Ni_{x\%}Al_2O_3$ (curves a-b, Figure 6B), it is tempting to conclude that carbon in these samples is mainly present in the form of Cγ graphite. Nevertheless, such carbon family is known as the most inert type of coke, strongly

contributing to deactivation by encapsulating the active sites and making them no longer accessible to gaseous reactants [64]. In view of the high catalytic stability of the samples (Figures 5A-C), such poisoning effect seems unlikely. Rather, as already proposed in the literature [65-67], we assume that the high temperature oxidation peak corresponds to less toxic transitory intermediate carbon species formed during gradual transformation of reactive $C\alpha$ and/or $C\beta$ into $C\gamma$. These species could be analogous to carbon nanotubes previously reported to form on nickel impregnated alumina catalysts during DRM without necessarily leading to catalyst deactivation [68], as will be indeed confirmed below by Raman, XRD and TEM/SEM data. The high temperature DSC peak almost vanished for the spent $Ni_{5\%}Mg_{5\%}Al_2O_3$ and $Ni_{5\%}Ca_{5\%}Al_2O_3$ samples (curves d and e, Figure 6B), in accordance with their very small $C_{(s)}$ content, and the peak slightly shifted towards lower temperature. Again, this is most probably due to the dynamic character (heating) of the analysis (as for TPR, see section 3.2), the maximum of the process (here an oxidation) occurring at slightly lower temperature when a lower amount of compound to be transformed is concerned. This is verified as well with the $Ni_{x\%}Al_2O_3$ series of samples having varying coke contents (curves a-c, Figure 6B). More remarkably, a low DSC temperature peak is distinctly identified for $Ni_{5\%}Mg_{5\%}Al_2O_3$ (and for $Ni_{5\%}Ca_{5\%}Al_2O_3$ to a lesser extend) in spite of the overall weak signal intensity (curve e, Figure 6B), revealing carbon deposition mainly as non-poisoning amorphous $C\alpha$ in this sample bearing a basicity promoter additive.

The transitory amorphous (rather than highly crystalline) state of carbon deposits in the $Ni_{x\%}Al_2O_3$ catalysts was also confirmed by Raman spectroscopy. Exploitable signals were obtained only for the spent $C_{(s)}$ richest $Ni_{7.5\%}Al_2O_3$ and $Ni_{10\%}Al_2O_3$ catalysts, otherwise the carbon species were not entirely covering the alumina particles and a strong fluorescence background, as often observed with microporous zeolites [69] or mesoporous silica or alumina [70] was hampering correct data detection. The two main bands in the spectra (Figure 8) were typical of the doubly degenerated phonon mode of C atoms in sp^2 carbon networks with high degree of symmetry and of order (graphitic carbon, G-band, 1601 cm^{-1}) and of a disordered structural mode of carbon species (D-band, 1312 cm^{-1}) [71-73]. The intensity ratio between these two bands (I_D/I_G) is often used as an indicator of the crystalline degree and/or presence of defects in the carbon species, the smaller the ratio (less than 1) the higher the structural order [71,73]. The ratio significantly higher than unity for both spent $Ni_{7.5\%}Al_2O_3$ and $Ni_{10\%}Al_2O_3$ (1.53 and 1.52, respectively) supports the assumption of the disordered (rather than well-ordered crystalline graphitic) character of the carbon deposits.

This is also in accordance with the peaks at circa 2700 and 2900 cm^{-1} (labeled 2D and (D+G) bands, respectively, Figure 8) that were recently reported, for poorly crystalline carbon containing samples (with I_D/I_G = 1.05), to provide further evidence of the presence of disorder and/or of defects in the carbon sp^2 species [74].

3.7 Morphological aspects and preservation of Ni dispersion during reaction

The shape of the coke deposits was next identified by electron microscopy that also provided important information on the morphology of porous networks and on nickel dispersion and location in the spent catalysts. Typical SEM (Figures 9A,B) and TEM (Figures 9C,D) images are shown for spent Ni$_{10\%}$Al$_2$O$_3$ taken as most representative (Ni-richest and C$_{(s)}$-richest) material. In this sample, long-carbon filaments are clearly identified (detected by both SEM and TEM) on the external surface of the alumina-based grains, some grains appearing slightly more covered than others. Ni nanoparticles developing coke are also visible, located either at the interface between the support and the grown filament or embedded into it. In some case, a peculiar "bamboo shape" due to the formation of several adjacent compartments can be recognized. This resembles the reported nucleation of carbon nanotubes with "close end" having a nanoparticle either at their bottom or within their tip [67,68,75].

Notably, the diameter of the carbon nanowires is close to that of the metal particles on which they grew, the nanoparticle being itself sintered compared to the nanoparticles that are still occluded inside the walls or the pores of alumina. This is a strong argument in favour of a main participation of external metal nanoparticles to the growth of carbon nanotubes, some Ni^0 particles thus suffering of simultaneous sintering and encapsulation in carbon species during the run. Nevertheless, they appear much less numerous, by far, than the highly dispersed Ni^0 nanoparticles remaining occluded within the mesopores of the alumina-based network (Figures 9C,D and Figure 10).

From microtome TEM images, it is clear that the uniform channel system and its ordered hexagonal organization (porous network) is quite well preserved, both along [110] (Figures 10A, B,B') and perpendicular to [001] (Figures 10A',C,C') grain directions, even after 40 h run at 800 °C under reactants (including steam). This excellent structural resistance is also attested by the N$_2$-sorption data of spent Ni$_{10\%}$Al$_2$O$_3$ (taken as example) after its re-calcination at 800 °C for coke removal (Figure 11) and by the persistence of low angles XRD peaks in the patterns for all spent catalysts (Figure 12A). From sorption data, some textural collapse is noted after reduction

(curve b, Fig. 11), accentuated after catalysis (curve c, Figure 11), but the spent catalyst still exhibits a well-defined type IV isotherm. This collapse could be related to a phase transition of the alumina substrate from mainly amorphous to more crystalline γ-phase as suggested by the XRD patterns of reduced and spent catalysts (Figure 12B) where peaks typical of crystalline γ-Al_2O_3 are visible, whatever the sample. This indicates a transition from amorphous into crystalline γ-alumina of (at least part of) the alumina phase at the high temperatures applied (800 °C), and the phenomenon is slightly accentuated after catalysis (patterns b'-d', Figure 12B) in line with longer heating treatment. Note, however, the absence of any intense and thin XRD peak (and therefore absence of formation of a bulky crystalline phase), which reveals a satisfying structural resistance of the organized alumina-based networks, in spite of the drastic conditions of reaction. Thus, the loss in surface area and pore volume (values in Table 1) are of about 15% (after reduction) and 50 % (after catalysis) but the pore size distributions remain unchanged. The collapse would therefore consist more in a progressive blocking of part of the pores rather than in a general shrinkage of the channels. In spite of such textural loss, many pores (half of initial ones after 800 °C/40 h reaction) remain open and accessible to reactants.

The other remarkable information resides in the numerous tiny Ni^0 nanoparticles that appear confined and well stabilized within the channels or even, in some cases, integrated within the alumina walls (Figures 10B,B',C,C'). This reveals some nickel sintering during high temperature treatments, as also confirmed by the weak XRD peaks typical of fully reduced Ni^0 with face centered cubic (FCC) unit cell (ICDD file # 65-0380) that become detectable (indexed   in Figure 12B) after reduction (patterns a-f) and are only scarcely modified after catalysis (patterns b'-f'), showing that the metal nanoparticles remain stable during the run. The average sizes of the Ni^0 particles deduced from these signals are in accordance with those estimated from TEM data (Table 6). In spent $Ni_{10\%}Al_2O_3$, the nickel nanoparticles have a mean diameter around 7 nm (as estimated from particle size counting), much smaller than those commonly reported (above 20 nm) for Ni-impregnated alumina catalysts (even mesoporous ones) after CSDRM run [15,44]. The mean size is even smaller (5-6 nm) in the 5 wt% Ni containing catalysts, independently on the presence or not of Mg or Ca additive (Table 6). Such difference could be due to the total absence of sintered Ni^0 nanoparticles on the external surface of the alumina grains while few with sizes as high as 20 nm were detected in the Ni richest spent $Ni_{10\%}Al_2O_3$ (as exemplified in Figure 10A).

Note also the absence of XRD signal attributable to graphitic deposits (expected around 2Θ~29°), even for $C_{(s)}$ richest $Ni_{10\%}Al_2O_3$ (pattern d', Figure 12B) that agrees with the negligible content of crystalline carbon in the spent catalysts deduced above from Raman data. Moreover, carbon deposits are not seen inside the preserved porous networks (TEM pictures).

3.8 Combined factors ensuring catalytic stability in CSDRM

From all above data, it can be concluded that the combination of "one-pot" synthesis (carried out in presence of Ni) with the "EISA" method (performed in presence of a structuring agent for generating ordered porosity) allowed to obtain, in a single step synthesis procedure, highly effective catalysts still exhibiting an organized mesoporous network and a highly dispersed Ni^0 active phase even after 40 h of CSDRM testing at 800 °C under reactants. The "one-pot" methodology permitted to fully introduce nickel in the materials, from the first step of their preparation, in the form of tiny species, possibly spinel-like ones, that are kept mainly embedded in the alumina-based walls after calcination at 450 °C (not detected by XRD, neither by TEM, data to be published). Even if part (or all) nickel is extracted from the ordered oxide matrices during reduction (Ni^0 nanoparticles in the pores, as seen by TEM), the formed metal nanoparticles remain predominantly (if not fully) trapped inside the pores where they benefit of the surrounding oxide porous network that protects them against sintering. Notably, such confinement is also beneficial with respect to resistance of the reduced Ni^0 nanoparticles to re-oxidation (not detected in our spent catalysts). Comparable stability effects were recently claimed in the case of "one-pot" synthesized oxide-based catalysts tested in DRM [43,45,51,52,61] or in SRM [46], but such types of materials were never considered yet in the combined CSDRM reaction that involves much more drastic conditions (especially steam and high temperatures). Moreover, the present method introducing the active phase (Ni) and the structuring agent (P123 Pluronic triblock copolymer) in a same synthesis batch was, to our knowledge, never considered regarding nickel-alumina based mesoporous catalysts. Nevertheless, it provides confinement effects that appear to be key factors for ensuring the stability of the catalysts.

Even if the nickel-alumina based $Ni_{x\%}Al_2O_3$ catalysts already offer high activity levels (Table 5) and excellent stability (Figure 5), the catalytic performances are further improved by adding an additive such as Mg (or to a lesser extend Ca). From the close Ni^0 nanoparticles sizes found in all 5 wt% Ni catalysts, whatever their composition (Table 6), it is clear that the additives do not play any role towards nickel dispersion or stabilization, as was already proposed [60]. Similarly, they have no

beneficial effect in term of porous network stabilization since the materials show lower specific surface area and pore volumes than the analogous additive-free sample (Table 2). Rather, their positive impact on activity levels (Figures 5 and 7, Table 5) resides in their propensity to provide some basicity (61) to the mixed additive-alumina-based oxide. This enhances CO_2 and H_2O activation and helps limiting the side reactions that can still occur at the high temperature of reaction., as seen from the enhanced selectivity towards metgas (molar H_2/CO product ratio close to 2, Figure 5C') and from the drastic reduction of carbon contents in the spent catalysts (Figure 6A and 7, Table 5). Note that the latter effect is important on an industrial point of view because carbon deposition is known to potentially lead to reactors blockage with time.

The beneficial basicity effect can be understood by considering some mechanistic aspects already established for SRM and DRM on Ni, Ru, Rh, Pd, Ir and Pt based catalysts supported on magnesia [76]. It was proposed that these two reactions involve similar mechanisms and that reforming rates are essentially limited by C-H bond activation on metal (here Ni) surfaces, identified as an irreversible process contrarily to CO_2 and H_2O activations that are reversible [77-79]. Several activation elementary steps (eq. 1- eq. 11) were distinguished [77-80], which also stand for CSDRM. They involve the generation of adsorbed activated (i) carbon (C^*, succession of eq. 1 to 4), (ii) hydrogen (H^*, eq. 2 to 4), (iii) carbon monoxide (CO*, eq. 6 then 7) and oxygen (O^*, eq. 5 and 7). These activated species next react together (eq. 9 to 11) to produce the expected gaseous CO and H_2 compounds. By facilitating H_2O and CO_2 dissociation [26,30,37], basicity enhances the formation of surface activated O* that can then react with neighbour adsorbed C*, thus inhibiting (or reducing) the participation of the latters to carbon polymerization phenomena that otherwise take place leading to coke [80]. In view of the high carbon contents in the spent $Ni_{x\%}Al_2O_3$ series of samples (Table 5), such coke deposits are formed at a significant extent in the less basic alumina-based materials (with no additives). This can be interpreted in term of a faster overall process of CH_4 decomposition and carbon polymerization (RI, Table 7 and Figure 13) compared to CO_2 and H_2O activation (RII and RIII, respectively). By contrast, all reactions rates would be of the same order on more basic catalysts (Figure 13). Remarkably, even when they exist at a significant amount, the coke deposits are only present as nanotubes grown on few external isolated (and sintered) Ni^0 nanoparticles located at the surface of the alumina grains (Figure 9), and they are not detrimental to catalytic stability (Figure 5) because they remain outside the

pores, far away from the Ni^0 nanoparticles that are kept occluded inside the pores, still accessible and active towards the reactants (Figure 10).

4. CONCLUSIONS

Ordered mesoporous nickel alumina (5-10 wt% Ni) materials eventually loaded with an additive (5 wt% Mg or Ca) were easily synthesized by a one-step procedure involving an evaporation-induced self-assembly strategy in presence of both an active phase (nickel) and a structuring agent. All nickel introduced in the synthesis medium was incorporated within the oxide matrix and this took place together with the structuration of the material in the form of well-organized channel networks. Upon reduction treatment needed to form the Ni^0 active phase, nickel is (at least partially) extracted from the alumina matrix but the nanoparticles remain predominantly (if not fully) occluded in the pores. The resulting high Ni^0 dispersion, together with a high resistance of the mesoporous network along 40 h of catalytic run at 800 °C under the harsh conditions of combined steam and dry methane reforming, appear as key factors leading to highly active and extremely stable catalysts. The catalytic performances are further enhanced by Mg (and to a lesser extent Ca) addition, but none of these two additives has an effect on structural features, neither on active phase dispersion. Rather, they play an effective role towards avoiding side reactions (nanotubes formation) and yielding high selectivity to metgas with a stable H_2/CO molar product ratio kept close to 2 in the exhaust gas. In their absence, some side reactions take place, especially methane decomposition that leads to the formation of elongated carbon nanotubes, grown on one (or several) sintered Ni^0 particle, which are however weakly poisoning (no effect on catalytic stability) because they remain at the exterior of the alumina grains, far away from the numerous active Ni^0 nanoparticles confined in the pores. The beneficial effect of nickel confinement in the pores is therefore twofold, consisting in protecting the metal nanoparticles against sintering but also against coking in their neighbouring due to steric constraints. In view of their effective textural, structural and catalytic performances, the "one-pot" mesoporous catalysts presented in this study represent ideal candidates for catalyzing metgas (or more generally syngas) production from biogas and/or biomass natural resources.

ACKNOWLEDGMENTS

REFERENCES

[1]   J.D. Figueroa, T. Fout, S. Plasynski, H. Mcllvried, R.D. Srivastava, Int. J. Greenhouse Gas Control 2 (2008) 9-20.

[2]   W. Wang, S. Wang, X. Ma, J. Gong, Chem. Soc. Rev. 40 (2011) 3703-3727.

[3]   G.A. Olah, G.S. Prakash, A. Goeppert, M. Czaun, T. Mathew, J. Am. Chem. Soc. 135 (2013) 10030-10031.

[4]   G.A. Olah, A. Goeppert, M. Czaun, T. Mathew, R.B. May, G.K.S. Prakash, J. Am. Chem. Soc. 137 (2015) 8720-8729.

[5]   G.A. Olah, A. Goeppert, M. Czaun, G.K.S. Prakash, J. Am. Chem. Soc. 135 (2013) 648-650.

[6]   G.A. Olah, A. Goeppert, G.K.S. Prakash, Beyond oil and gas: the methanol economy 2011, John Wiley and Sons.

[7]   G.A. Olah, GPrakash, G.K.S. US Pat. 2013, 8,440,729.

[8]   G.A.Olah, G.K.S. Prakash, US Pat. 2014, 8,697,759.

[9]   G.A. Olah, G.K.S. Prakash, US Pat. 2015, 8,980,961.

[10] G.A. Olah, G.K.S. Prakash, European Pat. 2010, 2,167,451A1.

[11] M.C.J. Bradford, M.A. Vannice, Catal. Rev.Sci. Eng. 41 (1999) 1-42.

[12] F. Pompeo, N.N. Nichio, M.M.V.M. Souza, D.V. Cesar, O.A. Ferretti, M. Schmal, Appl. Catal. A: Gen. 316 (2007) 176-183.

[13] T.V. Choudhary, V.R Choudhary, Angew. Chem. Int. Ed. 47 (2008) 1828-1847.

[14] M.S. Fan, A.Z. Abdullah, S. Bhatia, ChemCatChem 1 (2009) 192-208.

[15] K. Jabbour, N. El Hassan, A. davidson, S. Casale, P. Massiani, Catal. Sci. Technol. 2016, DOI: 10.1039/C6CY00032K.

[16] D. Qin, J. Lapszewicz, X.J. Jiang, Catal. 159 (1996) 140-149.

[17] D. Qin, J. Lapszewicz, J. Catal. Today 21 (1994) 551-560.

[18] M.A. Soria, C. Mateos-Pedrero, A. Guerrero-Ruiz, I. Rodríguez-Ramos, Int. J. Hydrogen Energy 36 (2011) 15212-15220.

[19] F. Yagi, A. Nagumo, Y. Wada, M. Shimura, US Pat. 2002, 6387843B1.

[20] Ş. Özkara-Aydınoğlu, Int. J. Hydrogen Energy 35 (2010) 12821- 12828.

[21] Y. Sun, T. Ritchie, S.S. Hla, S. McEvoy, W. Stein, J.H. Edwards, J. Nat. Gas. Chem. 20 (2011) 568-576.

[22] M. Jafarbegloo, A. Tarlani, A.W. Mesbah, S. Sahebdelfar, Int. J. Hydrogen Energy 40 (2015) 2445-2451.

[23] B.A. Santos, J.M. Loureiro, A.M. Ribeiro, A.E. Rodrigues, A.F. Cunha, Can. J. Chem. Eng. 93 (2015) 510-526.

[24] K.Y. Koo, H.S. Roh, Y.T. Seo, D.J. Seo, W.L. Yoon, S.B. Park, Int. J. Hydrogen Energy 33 (2008) 2036–2043.

[25] I.H. Son, S.J. Lee, A. Soon, H.S. Roh, H. Lee, Appl. Catal. B: Env. 134 (2013) 103-109.

[26] K.Y. Koo, H.S. Roh, Y.T. Seo, D.J. Seo, W.L. Yoon, S.B. Park, Appl. Catal. A: Gen. 340 (2008) 183-190.

[27] H.S. Roh, K.Y. Koo, U.D. Joshi, W.L. Yoon, Catal. Lett. 125 (2008) 283-288.

[28] K.Y. Koo, H.S. Roh, U.H. Jung, W.L. Yoon, Catal. Today 185 (2012) 126-130.

[29] M. García-Diéguez, I.S. Pieta, M.C. Herrera, M.A. Larrubia, L.J. Alemany, Catal. Today 175 (2011) 136-142.

[30] J. Mehz, K.J. Jozani, A.N. Pour, Y. Zamani, React. Kinet. Catal. Lett. 75 (2002) 267-273.

[31] K.M. Kang, I.W. Shim, H.Y. Kwak, Fuel Process. Technol. 93 (2012) 105-114.

[32] K.Y Koo, S.H. Lee, U.H. Jung, H.S. Roh, W.L. Yoon, Fuel Process. Technol. 119 (2014) 151-157.

[33] K.Y. Koo, H.S. Roh, U.H. Jung, D.J. Seo, Y.S. Seo, W.L. Yoon, Catal. Today 146 (2009) 166-171.

[34] S.C. Baek, J.W. Bae, J.Y. Cheon, K.W. Jun, K.Y. Lee, Catal. Lett. 141 (2011) 224-234.

[35] J.W. Bae, A.R. Kim, S.C. Baek, K.W. Jun, React. Kinet. Catal. Lett. 104 (2011) 377-388.

[36] A.N. Pour, Y.Z. Kheirolah, J. Jozani, J.Y. Mehr, React. Kinet. Catal. Lett. 86 (2005) 157-162.

[37] H.S. Roh, K.Y. Koo, J.H. Jeong, Y.T. Seo, D.J. Seo, Y.S. Seo, W.L. Yoon, S.B. Park, Catal. Lett. 117 (2007) 85-90.

[38] H.S. Roh, K.Y. Koo, W.L. Yoon, Catal. Today 146 (2009) 71-75.

[39] B. Huang, X. Li, S. Ji, B. Lang, F. Habimana, C. Li, J. Nat. Gas Chem. 17 (2008) 225-231.

[40] M.N. Kaydouh, N. El Hassan, A. Davidson, S. Casale, H. El Zakhem, P. Massiani, Microporous Mesoporous Mater. 220 (2016) 99-109.

[41] M.N. Kaydouh, N. El Hassan, A. Davidson, S. Casale, H. El Zakhem, P. Massiani, C.R. Chim. 18 (2015) 293-301.

[42] A. Albarazi, M.E. Gálvez, P. Da Costa, Catal. Comm. 59 (2015) 108-112.

[43] N. Wang, Z. Xu, J. Deng, K. Shen, X. Yu, W. Qian, W. Chu, F. Wei, ChemCatChem 6 (2014) 1470-1480.

[44] X. Fang, C. Peng, H. Peng, W. Liu, X. Xu, X. Wang, C. Li, W. Zhou, ChemCatChem 7 (2015) 3753-3762.

[45] L. Xu, H. Sonf, L. Chou, Catal. Sci. Technol. 1 (2011) 1032-1042.

[46] W. Shen, K. Komatsubara, T. Hagiyama, A. Yoshida, S. Naito, Chem. Comm. 42 (2009) 6490-6492.

[47] S.M. Morris, P.F. Fulvio, M. M. Jaroniec, J. Am. Chem. Soc. 130 (2008) 15210-15216.

[48] Q. Yuan, A.X. Yin, C. Luo, L.D. Sun, Y.W. Zhang, W.T. Duan, H.C. Liu, C.H. Yan, J. Am. Chem. Soc. 130 (2008) 3465-3472.

[49] M. M. Naira, S. Kaliaguine, New J. Chem. 40 (2016) 4049-4060.

[50] F. Chen, C. Wu, L. Dong, A. Vassallo, P.T. Williams, J. Huang, Appl. Catal. B: Env. 183 (2016) 168-175.

[51] L. Xu, H. Song, L. Chou, Appl. Catal. B: Env. 108 (2011) 177-190.

[52] L. Xu, H. Song, L. Chou, ACS Catalysis 2 (2012) 1331-1342.

[53] S.T. Harding, C.A. Floudas, AIChE Journal 46 (2000) 1422-1440.

[54] W. Cai, J. Yu, C. Anand, A. Vinu, M.M. Jaroniec, Chem. Mater. 23 (2011) 1147-1157.

[55] A. Grosman, C. Ortega, Langmuir 24 (2008) 3977-3986.

[56] J. Zhang, H. Xu, X. Jin, Q. Ge, W. Li, Appl. Catal. A: Gen. 290 (2005) 87- 96.

[57] J.A.C. Dias, J.M. Assaf, Catal. Today 85 (2003) 59-68.

[58] S.Y. Chen, C.Y. Tang, J.F. Lee, L.Y. Jang, T. Tatsumi, S.J. Cheng, J. Mater. Chem. 21 (2011) 2255-2265.

[59] J. Rostrup-Nielsen, L.J. Christiansen, Concepts in Syngas Manufacture Imperial College Press: London 2011.

[60] M. Nichele, V. Signoretto, F. Pinna, F. Menegazzo, I. Rossetti, G. Cruciani, G. Cerrato, A. Di Michele, Appl. Catal. B: Env. 150 (2014) 12-20.

[61] N. Wang, K. Shen, L. Huang, X. Yu, W. Qian, W. Chu, ACS Catalysis 3 (2013) 1638-1651.

[62] J.M. García-Vargas, J.L. Valverde, J. Díez, P. Sánchez, F. Dorado, Appl. Catal. B: Env. 148 (2014) 322-329.

[63] J.Z. Luo, Z.L. Yu, C.F. Ng, C.T. Au, J. Catal. 194 (2000) 198-210.

[64] J. Guo, H. Lou, X.M. Zheng, Carbon 45 (2007) 1314-1321.

[65] Z.L. Zhang, X.E. Verykios, Catal. Today 21 (1994) 589-595.

[66] M.D. Argyle, C.H. Bartholomew, Catalysts 5 (2015) 145-269.

[67] L. Zhou, L. Li, N. Wei, J. Li, J.M. Basset, ChemCatChem 16 (2015) 2508-2516.

[68] D. Chen, K.O. Christensen, E. Ochoa-Fernandez, Z. Yu, B. Tøtdal, N. Latorre, A. Monzon, A. Holmen, J. Catal. 229 (2005) 82-96.

[69] L.I. Meza, M.W. Anderson, J.R. Agger, C.S. Cundy, From Zeolites to Porous MOF Materials-The 40th, Anniversary of International Zeolite Conference: In Proceedings of the 15th International Zeolite Conference 2007.

[70] C.Y. Chen, H.X. Li, M.E. Davis, Microporous Mater. 2 (1993) 17-26.

[71] D. Liu, X.Y. Quek, W.N.E. Cheo, R. Lau, A. Borgna, Y. Yang, J. Catal. 266 (2009) 380-390.

[72] M. Che, J.C. Vedrine, Characterization of Solid Materials and Heterogeneous Catalysts, 2012, Wiley-VCH, pp 64-67.

[73] C. Pan, Q. Bao, J. Mater. Sci. Lett. 21 (2002) 1927-1929.

[74] E.C. Vermisoglou, T. Giannakopoulou, G. Romanos, M. Giannouri, N. Boukos, C. Lei, C. Lekakou, C. Trapalis, Appl. Surf. Sci. 358 (2015) 100-109.

[75] T.V. Choudhary, E. Aksoylu, D.W. Goodman, Catal. Rev. Sci. Eng. 45 (2003) 151-203.

[76] J.R. Rostrup-Nielsen, J.H. Bak Hansen, J. Catal. 144 (1993) 38-49.

[77] J. Wei, E. Iglesia, J. Phys. Chem. B 108 (2004) 4094-4103.

[78] J. Wei, E. Iglesia, J. Catal. 224 (2004) 370-383

[79] A. Donazzi, A. Beretta, G. Groppi, P. Forzatti, J. Catal. 255 (2008) 259-268.

[80] T.H. Nguyen, A. Lamacz, A. Krzton, B. Liszka, G. Djéga-Mariadassou, Appl. Catal. B 182 (2016) 385-391.

Table 1. Bibliographic listing of the different types of supported Ni-based catalysts and their performances in CSDRM

Cat.[a]	S.A.[b]	Ni wt%	Co-metal, wt%	Rr[c]	T (°C)	GHSV (L.g$_{cat}^{-1}$.h^{-1})	Initial performance XCH$_4$ (%)	Initial XCO$_2$ (%)	Initial H$_2$/CO	TOS (h)[d]	deac.[e]	Final performance XCH$_4$ (%)	Final XCO$_2$ (%)	Final H$_2$/CO	Ref
Ni/Al$_2$O$_3$	107	12	---	1/0.4/0.8	750	530	71	n.m.		20	C,S.	64	n.m.		26
Ni/MgO-Al$_2$O$_3$	70	12	MgO, 20				76					75			
Ni/Al$_2$O$_3$	n.m.	12	---	1/0.4/0.8/1	800	265	81	n.m.	7	32	C	n.m.		n.m.	27
Ni-CeO$_2$-ZrO$_2$	97	15	Ce$_{80}$Zr$_{20}$				97	80	1.9	20	---	95	78		
Ni/Al$_2$O$_3$	3	12	---	1/0.4/0.8/1	700	530	62	40	n.m.	20	C, S	18	12	n.m.	28
Ni-Ce/Al$_2$O$_3$	10	12	CeO$_2$, 6				72	57	n.m.		---	70	43	n.m.	
Ni/Al$_2$O$_3$	n.m.	4	---	1/0.3/0.7/3	750	60	89	49	1.49	14	n.m.	89	49	1.49	29
Ni-Rh/Al$_2$O$_3$		4	Rh, 0.04				89	44	1.63			89	44	1.63	
Ni/Al$_2$O$_3$	n.m.	15	---	1/1/0.16	750	n.m.	95	90	0.9	n.m.	C, S		n.m.		30
Ni/MgO-Al$_2$O$_3$			MgO, 15				100	92	1.1						
Ni-Al$_2$O$_3$	n.m.	10	---	1/0.3/0.7	800	30	92	76	2.70	50	C	92	75	2.70	31
Ni-MgO-Al$_2$O$_3$			MgO, 15				94	74	2.80		---	94	74	2.80	
Ni/MgO-Al$_2$O$_3$	n.m.	10	---	1/0.4/0.8/1	700	530	77	62	2.20	16	C		n.m.		32
Ni-Ce/MgO-Al$_2$O$_3$[*]	26		CeO$_2$, 2.5				81	66	2.1		---				
Ni/MgO-Al$_2$O$_3$	108	12	MgO, 70	1/0.4/0.8/1	750	530	97	71	2.3	5	C, S	97	71	2	33
	112		MgO, 30				97	84	2		---	97	84	2	
Ni/MgO-Al$_2$O$_3$[*]	118	12	---	1/0.4/1/1	850	n.m.	85[+]	47[+]	2.27[+]		C, S	81[+]	44[+]	2.8[+]	34
Ni-Ce/MgO-Al$_2$O$_3$[*]	117	12	CeO$_2$, 4				86[+]	58[+]	2.15[+]	20	---	83[+]	52[+]	2.2[+]	
Ni/MgO-Al$_2$O$_3$[*]	118	15	---	1/0.4/1/1	850	n.m.	74[+]	35[+]	2.22[+]		C, S	77[+]	32[+]	2.19[+]	35
Ni-Ce-Zr/MgO-Al$_2$O$_3$ f	137	15	Ce$_{80}$Zr$_{20}$, 15				81[+]	44[+]	2.29[+]	20	---	81[+]	41[+]	2.24[+]	
Ni/MgO-Al$_2$O$_3$[*]	80	15	---	1/1/0.16	750	n.m.	95	90	n.m.	n.m.	C		n.m.		36
Ni-La/MgO-Al$_2$O$_3$[*]	81		La$_2$O$_3$, 10				100	95	n.m.		---				
Ni/MgO	6	12	---	1/0.4/0.8	800	265	60	n.m.		20	C	56	n.m.		37
Ni/Al$_2$O$_3$	4	n.m.					72			5		35			
Ni/CeO$_2$	9						57					46			
Ni/ZrO$_2$	17	12					64			20		73			
Ni/MgO-Al$_2$O$_3$	108		MgO, 30				92				---	89			
Ni/CeO$_2$	9	15	---	1/0.4/0.8	800	265	58	n.m.		20	C, S	47	n.m.		38
Ni/ZrO$_2$	17		---				78				C, S	63			
Ni/CeO$_2$-ZrO$_2$	60		Ce$_{80}$Zr$_{20}$				94				C, S	82			
Ni/SBA-15	n.m.	10	---	1/0.5/0.75	850	27	98	86	1.74	600	C, S R	85	50	2.2	39
Ni/MgO-SBA-15			MgO, 3				98	91	1.71		R	98	79	1.9	

n.m. not mentioned

[a]: Catalysts (Cat.) are represented based on the Ni deposition method: "Ni/" indicate a post-impregnation of Ni (and of the secondary metal) on the support and "Ni-" indicate a direct deposition of Ni (and of the secondary metal) in the course of support synthesis, [b]:Surface area (S.A.) of the catalyst, [c]: Molar composition of feeding reactants (CH$_4$/CO$_2$/H$_2$O/diluent (Ar or N$_2$)- mol/mol/mol/mol), [d]: Time on stream (TOS) defined as the duration of stability measurements at a fixed temperature, [e]: Deactivation (Deac.) is classified in terms of: Coke deposition (C), sintering (S) and/or reoxidation (R) of metallic nanoparticles, [*]: MgO$_{(x)}$-Al$_2$O$_{3(y)}$ support having a composition of x= 30% and y= 70%, [+]: Reaction conducted at P= 10 bar otherwise the operation pressure is 1 bar in the remaining tabulated studies

		N₂-sorption analysis						H₂-uptakes	
Sample	Ni and additive content (wt%)	BET specific surface area ($m^2.g^{-1}$)		Pore volume ($cm^3.g^{-1}$)		Average pore diameter (nm)**		Total H₂-uptake ($\mu mol.g^{-1}$)	
		calc.*	red.*	calc.*	red.*	calc.*	red.*	Exp.	The.
Al_2O_3	---	225	142	0.46	0.35	8± 4	8± 6	25	---
$Ni_{5\%}Al_2O_3$	5.0 Ni	215	111	0.45	0.33	9± 5	9± 5	941	900
$Ni_{7.5\%}Al_2O_3$	7.5 Ni	208	139	0.49	0.39	10± 6	10± 6	1339	1350
$Ni_{10\%}Al_2O_3$	10.0 Ni	201	180,101#	0.55	0.45,0.28#	11± 6	11,13#±6	1761	1800
$Ni_{5\%}Ca_{5\%}Al_2O_3$	5.0 Ni,5.0 Ca	157	105	0.42	0.36	12± 5	11± 5	945	900
$Ni_{5\%}Mg_{5\%}Al_2O_3$	5.0 Ni,5.0 Mg	169	115	0.44	0.40	12± 6	12± 5	928	

Table 2. Textural properties of calcined samples and H₂-uptakes during reduction.

*: Textural values after (calc.) calcination at 600°C for 5h and (red.) subsequent H₂-reduction at 800°C for 3h)

**: Average pore diameter ± standard deviation from the maxima

***: H₂-uptakes (Exp.) determined experimentally from TPR profiles after complete reduction at T=900°C and (The) theoretical values calculated from the expected Ni^{2+} content

#: Textural values obtained over the spent catalyst after re-calcination (450°C/5h) for removal of carbon deposits

Table 3. List of main and side-reactions [59] possibly occurring during combined steam and dry reforming of methane and probability of occurrence (Favorable or Not Favorable) as evaluated from thermodynamic calculations of the Gibbs free energy change (delta G) using the HSC 7.1 Chemistry software

Reactions	Equations	Temperature range (°C)			
		100-400	400-600	600-800	800-1000
		Zone 1*	Zone 2*	Zone 3*	Zone 4*
Reforming reactions					
Steam reforming of methane (SRM)	$CH_4 + H_2O \rightarrow 3H_2 + CO$	N.F.-F.	F.	F.	F.
Dry reforming of methane (DRM)	$CH_4 + CO_2 \rightarrow 2H_2 + 2CO$	N.F.	N.F. - F.	F.	F.
Combined steam and dry reforming of methane (CSDRM)	$CH_4 + 1/3CO_2 + 2/3 H_2O \rightarrow 8H_2 + 4CO$	N.F.	N.F.	N.F.-F.	F.
Side reactions (non-coke forming)					
Water gas shift (WGS)	$CO + H_2O \rightarrow CO_2 + H_2$	F.	F.	F.-N.F.	N.F.
Reverse water gas shift (RWGS)	$CO_2 + H_2 \rightarrow CO + H_2O$	N.F.	N.F.-F.	F.	F.-N.F.
CO_2 methanation	$CO_2 + 4H_2 \rightarrow CH_4 + 2H_2O$	F.	F.-N.F.	N.F.	N.F.
Side reactions (coke forming)					
CO_2 hydrogenation	$CO_2 + 2H_2 \rightarrow 2H_2O + C_s$	F.	F.-N.F.	N.F.	N.F.
CH_4 decomposition	$CH_4 \rightarrow 2H_2 + C_s$	N.F.	N.F.-F.	F.	F.-N.F.
CO disproportionation (Boudouard)	$2CO \rightarrow CO_2 + C_s$	F.	F.	F.-N.F.	N.F.
CO dehydrogenation	$CO + H_2 \rightarrow H_2O + C_s$	F.	F.-N.F.	N.F.	N.F.
Selectivity (H_2/CO molar ratio)		344-37.1	37.1-3.9	3.9-2.1	2.1-2.0

*: Temperature zones as identified on Figure 3A
F.: favored reaction
N.F.: not favored reaction
N.F.-F. (or F.-N.F.) : from not favored to favored (or reverse) on the considered zone

28

Table 4. Effect of reaction temperature on catalytic performance in combined steam and dry reforming of methane ($CH_4/CO_2/H_2O$= 1/0.4/0.8/12, P= 1atm, GHSV= 69 $L.g_{cat}^{-1}.h^{-1}$)

Samples	T= 600°C Conversion (%)				T= 700°C Conversion (%)				T= 800°C Conversion (%)			
	XCH_4		XCO_2		XCH_4		XCO_2		XCH_4		XCO_2	
	*	**	*	**	*	**	*	**	*	**	*	**
$Ni_{5\%}Al_2O_3$	37	24	---		45	43	22	15	57	54	51	43
$Ni_{7.5\%}Al_2O_3$	44	35	---		55	49	29	24	66	60	61	50
$Ni_{10\%}Al_2O_3$	64	60	---		78	71	56	49	82	80	80	76
$Ni_{5\%}Ca_{5\%}Al_2O_3$	45	35	---		60	54	53	44	69	65	61	57
$Ni_{5\%}Mg_{5\%}Al_2O_3$	58	54	---		70	66	40	34	77	73	72	70

Samples	T= 600°C H_2/CO (molar ratio)***		T= 700°C H_2/CO (molar ratio)***		T= 800°C H_2/CO (molar ratio)***	
	*	**	*	**	*	**
$Ni_{5\%}Al_2O_3$	4.3	4.3	2.6	2.9	2.2	2.4
$Ni_{7.5\%}Al_2O_3$	4.1	4.2	2.7	2.7	2.2	2.3
$Ni_{10\%}Al_2O_3$	4.1	4.2	2.4	2.5	2.3	2.4
$Ni_{5\%}Ca_{5\%}Al_2O_3$	4.2	4.2	2.5	2.6	2.1	2.2
$Ni_{5\%}Mg_{5\%}Al_2O_3$	4.1	4.1	2.6	2.6	2.1	2.1

Average values calculated over 3h step at each temperature passing from 800 down to 600°C (*) or from 600 up to 800°C (**) after *in-situ* H_2-reduction (800°C/3h).
***: The precision of the H_2/CO molar ratio value is at ± 0.05

Table 5. Conversions, products molar ratio and coke content over spent catalysts (40h) after combined steam and dry reforming of methane ($CH_4/CO_2/H_2O$= 1/0.4/0.8/12, T= 800°C, P= 1atm).

GHSV (L.g_{cat}^{-1}.h^{-1}, mass of catalyst)		Samples	Conversion (%)				Molar composition of main products		Coke content (wt%)*
			t= 1h		t= 40h		t= 1h	t= 40h	
			XCH_4	XCO_2	XCH_4	XCO_2	H_2/CO	H_2/CO	
	138 (50 mg)	$Ni_{5\%}Al_2O_3$	57	51	59	54	2.12	2.17	9
		$Ni_{7.5\%}Al_2O_3$	66	63	67	61	2.20	2.22	12
		$Ni_{10\%}Al_2O_3$	81	79	82	77	2.27	2.33	19
		$Ni_{5\%}Ca_{5\%}Al_2O_3$	64	58	65	58	2.09	2.05	4
		$Ni_{5\%}Mg_{5\%}Al_2O_3$	79	73	80	74	2.10	2.10	3
	69 (100 mg)	$Ni_{5\%}Al_2O_3$	81	76	82	77	2.12	2.10	6
		$Ni_{7.5\%}Al_2O_3$	85	81	87	81	2.11	2.16	7
		$Ni_{10\%}Al_2O_3$	89	85	88	83	2.20	2.23	9
Thermodynamic values			92	87	92	87	2.10	2.10	16

*: Determined from TGA/DTA analyses of 40h spent catalysts for the weight loss detected between 300-900°C

Table 6. Average particle size of nickel species in reduced (*in-situ* H_2-reduction, 800°C/3h) and spent ($CH_4/CO_2/H_2O$= 1/0.4/0.8/12, 800°C/40h, GHSV= 138 $L.g_{cat}^{-1}.h^{-1}$) catalysts

Samples	Reduced, Ø Ni^0(nm)		Spent, Ø Ni^0(nm)	
	XRD*	TEM	XRD*	TEM
$Ni_{5\%}Al_2O_3$	3.5	3.0**	5.8	5.5**
$Ni_{5\%}Ca_{5\%}Al_2O_3$	3.3	---	6.1	5.4
$Ni_{5\%}Mg_{5\%}Al_2O_3$	3.8	---	5.9	5.1
$Ni_{7.5\%}Al_2O_3$	4.7	---	6.5	---
$Ni_{10\%}Al_2O_3$	5.4	4.5	8.2	7.2

*: Calculated using Scherrer's equation at 2Θ= 51.8° for the [200] indexed plane, n.d.: not determined (broad peaks)
**: From our previous work [ref. 15]

Table 7. Adsorption activated mechanisms during DRM, SRM and CSDRM reactions [80]

Reaction type (and rate)	Mechanism	Equation number
CH$_4$ activation (R$_I$)	$CH_4 + 2* \rightarrow CH_3^* + *$	1
	$CH_3^* + * \rightarrow CH_2^* + H^*$	2
	$CH_2^* + * \rightarrow CH^* + H^*$	3
	$CH^* + * \rightarrow C^* + H^*$	4
H$_2$O activation (R$_{II}$)	$H_2O + * \rightarrow H_2 + O^*$	5
CO$_2$ activation (R$_{III}$)	$CO_2 + * \rightarrow CO_2^*$	6
	$CO_2^* + * \rightarrow CO^* + O^*$	7
	$CO^* \rightarrow CO + *$	8
Surface reactions	$C^* + O^* \rightarrow CO + 2*$	9
	$CO^* \rightarrow CO + *$	10
	$H^* + H^* \rightarrow H_2 + 2*$	11

Figure 1. (A) N$_2$ adsorption-desorption isotherms and (B) low and (C) wide angles XRD patterns of calcined samples: (a) Al$_2$O$_3$, (b) Ni$_{5\%}$Al$_2$O$_3$, (c) Ni$_{7.5\%}$Al$_2$O$_3$, (d) Ni$_{10\%}$Al$_2$O$_3$, (e) Ni$_{5\%}$Ca$_{5\%}$Al$_2$O$_3$ and (f) Ni$_{5\%}$Mg$_{5\%}$Al$_2$O$_3$. For XRD patterns, an offset was applied along *Y*-axis for the sake of clarity.
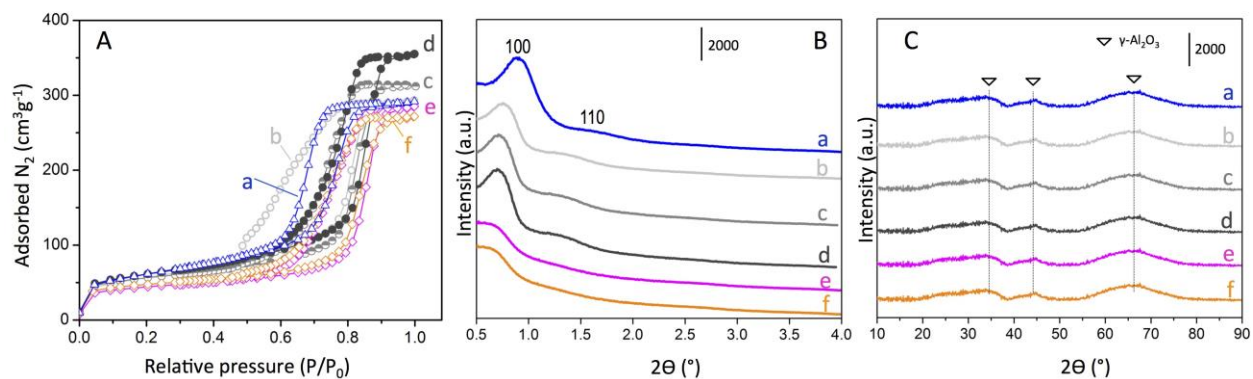
Figure 2. (A) H_2-TPR profiles and (B) total experimental H_2-uptake as a function of Ni content (wt%) for calcined alumina based samples: (a) Al_2O_3, (b) $Ni_{5\%}Al_2O_3$, (c) $Ni_{7.5\%}Al_2O_3$, (d) $Ni_{10\%}Al_2O_3$, (e) $Ni_{5\%}Ca_{5\%}Al_2O_3$ and (f) $Ni_{5\%}Mg_{5\%}Al_2O_3$.
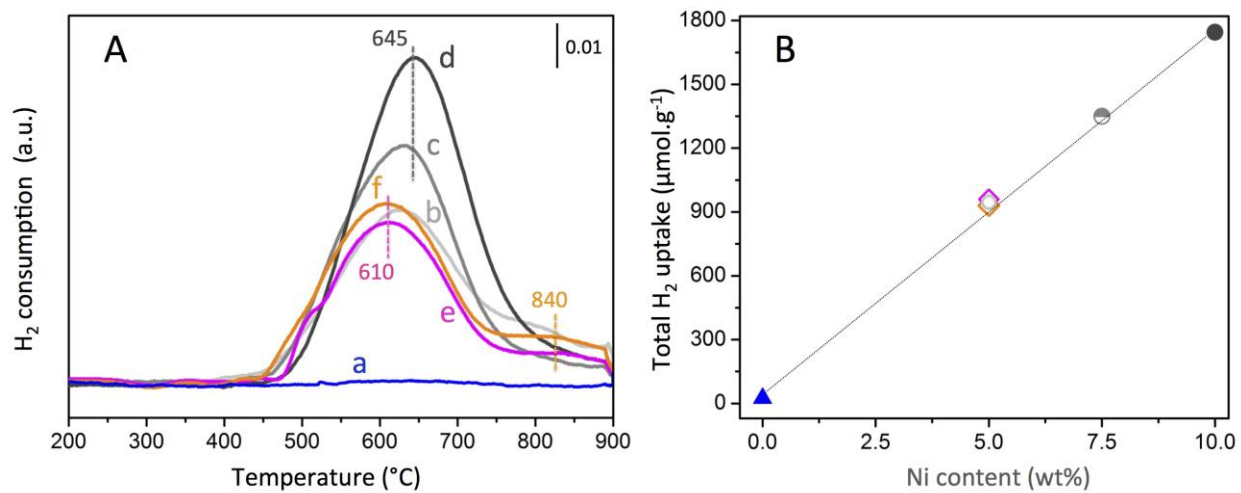
Figure 3. (A) Thermodynamic equilibrium plots (100-1000°C) and (B) related equilibrium conversions (CH$_4$ and CO$_2$) and molar product H$_2$/CO ratios (600-800°C) under CSDRM conditions; evaluations obtained from the HSC 7.1 chemistry software considering initial molar composition CH$_4$/CO$_2$/H$_2$O/Ar = 1/0.4/0.8/12 and including carbon C$_{(s)}$formation.
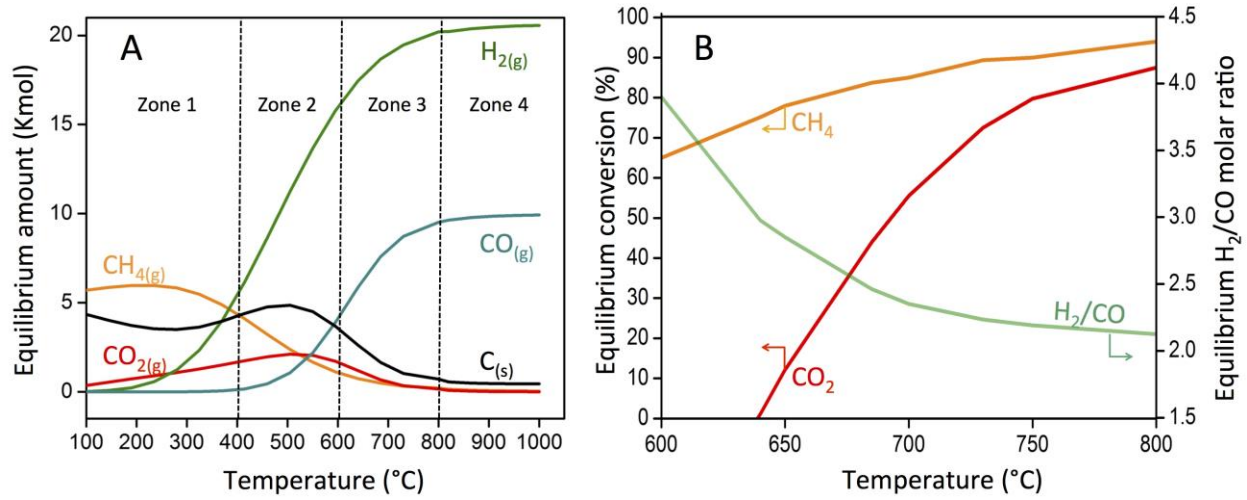
Figure 4. Evolutions of (A) CH_4 conversion, (B) CO_2 conversion and (C) H_2/CO molar product ratio upon stepwise decrease of temperature from 800 to 600°C during combined steam and dry reforming of methane (P = 1 atm, GHSV = 138 $L.g_{cat}^{-1}.h^{-1}$) over *in-situ* reduced (a) $Ni_{5\%}Al_2O_3$, (b) $Ni_{7.5\%}Al_2O_3$, (c) $Ni_{10\%}Al_2O_3$, (d) $Ni_{5\%}Ca_{5\%}Al_2O_3$ and (e) $Ni_{5\%}Mg_{5\%}Al_2O_3$. The thermodynamic values (dashed-lines) were calculated with the HSC 7.1 Chemistry software.
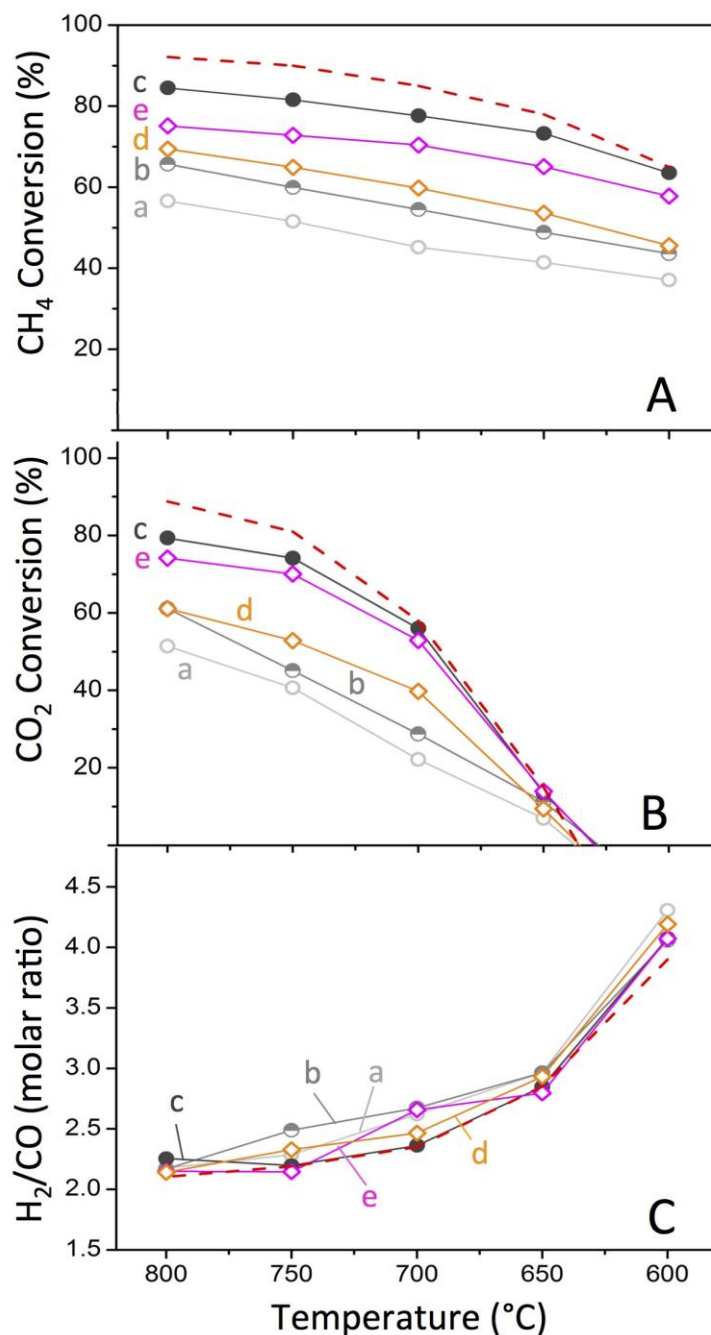
Figure 5. (A,A') CH_4 conversions, (B,B') CO_2 conversions and (C,C') H_2/CO molar product ratio during combined steam and dry reforming of methane at 800°C (P = 1 atm, GHSV = 138 $L.g_{cat}^{-1}.h^{-1}$) as a function of time-on-stream over: (a) $Ni_{5\%}Al_2O_3$, (b) $Ni_{7.5\%}Al_2O_3$, (c) $Ni_{10\%}Al_2O_3$, (d) $Ni_{5\%}Ca_{5\%}Al_2O_3$ and (e) $Ni_{5\%}Mg_{5\%}Al_2O_3$ catalysts. Thermodynamic values (dashed-lines) were calculated with the HSC 7.1 Chemistry software.
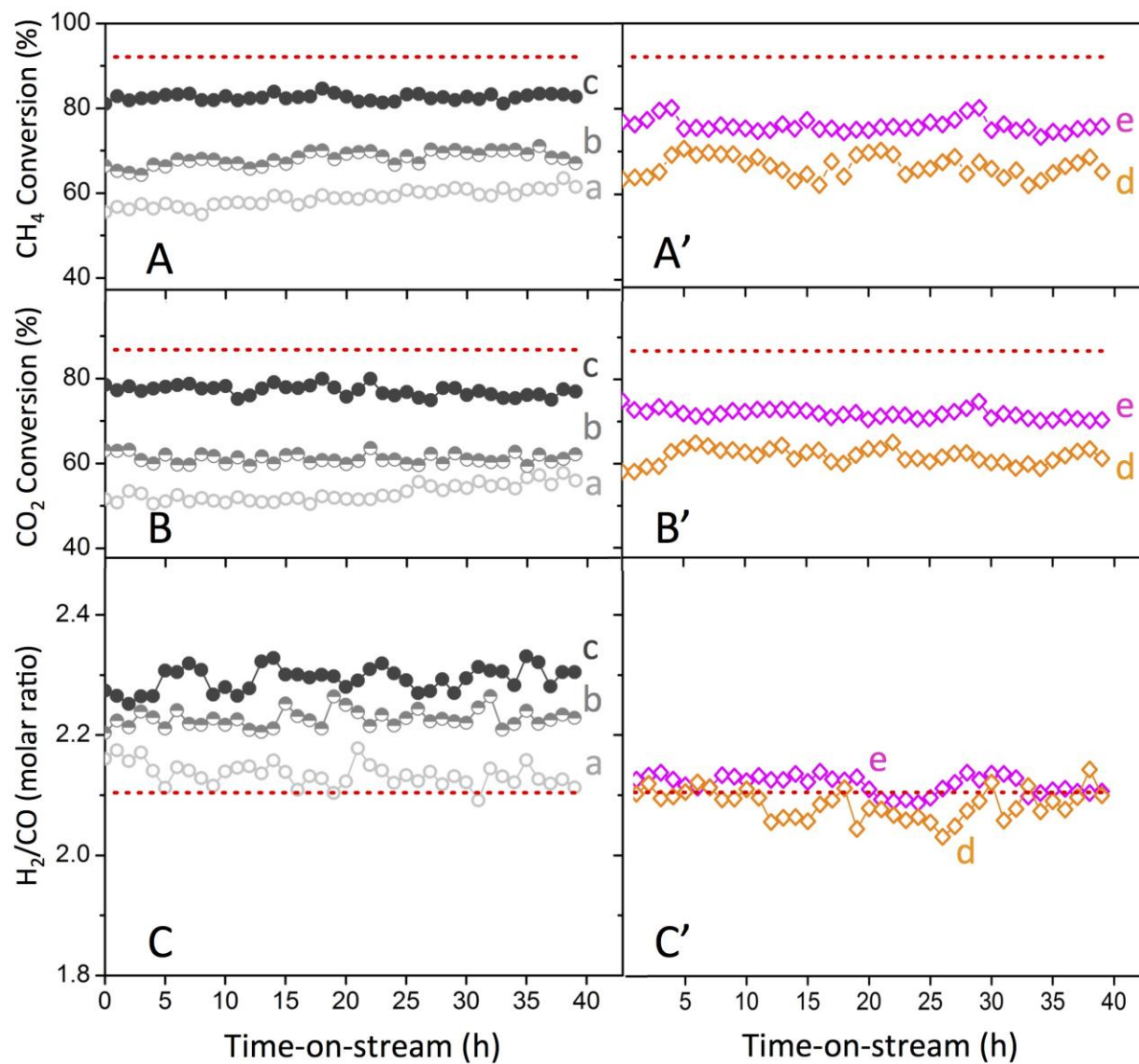
Figure 6. (A) TGA and (B) DSC profiles of spent (800°C/40h, $CH_4/CO_2/H_2O/Ar$ = 1/0.4/0.8/12, GHSV = 138 $L.g_{cat}^{-1}.h^{-1}$) catalysts: (a) $Ni_{5\%}Al_2O_3$, (b) $Ni_{7.5\%}Al_2O_3$, (c) $Ni_{10\%}Al_2O_3$, (d) $Ni_{5\%}Ca_{5\%}Al_2O_3$ and (e) $Ni_{5\%}Mg_{5\%}Al_2O_3$.
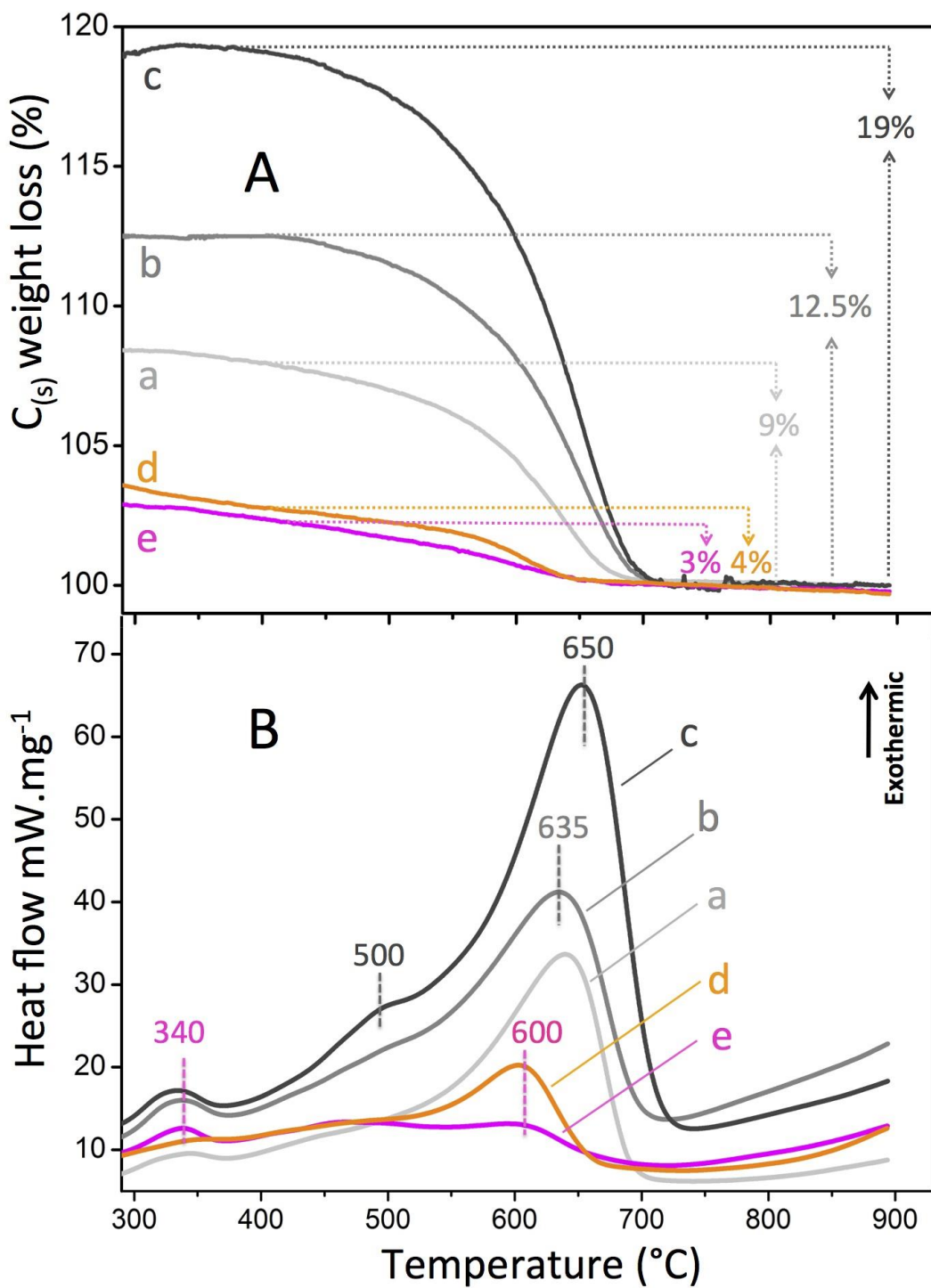
Figure 7: Correlation between reactivity levels (mean methane conversion) and coke deposition ($C_{(s)}$ wt%) along stability tests (800°C/40h, $CH_4/CO_2/H_2O/Ar$ = 1/0.4/0.8/12, GHSV = 138 $L.g_{cat}^{-1}.h^{-1}$).
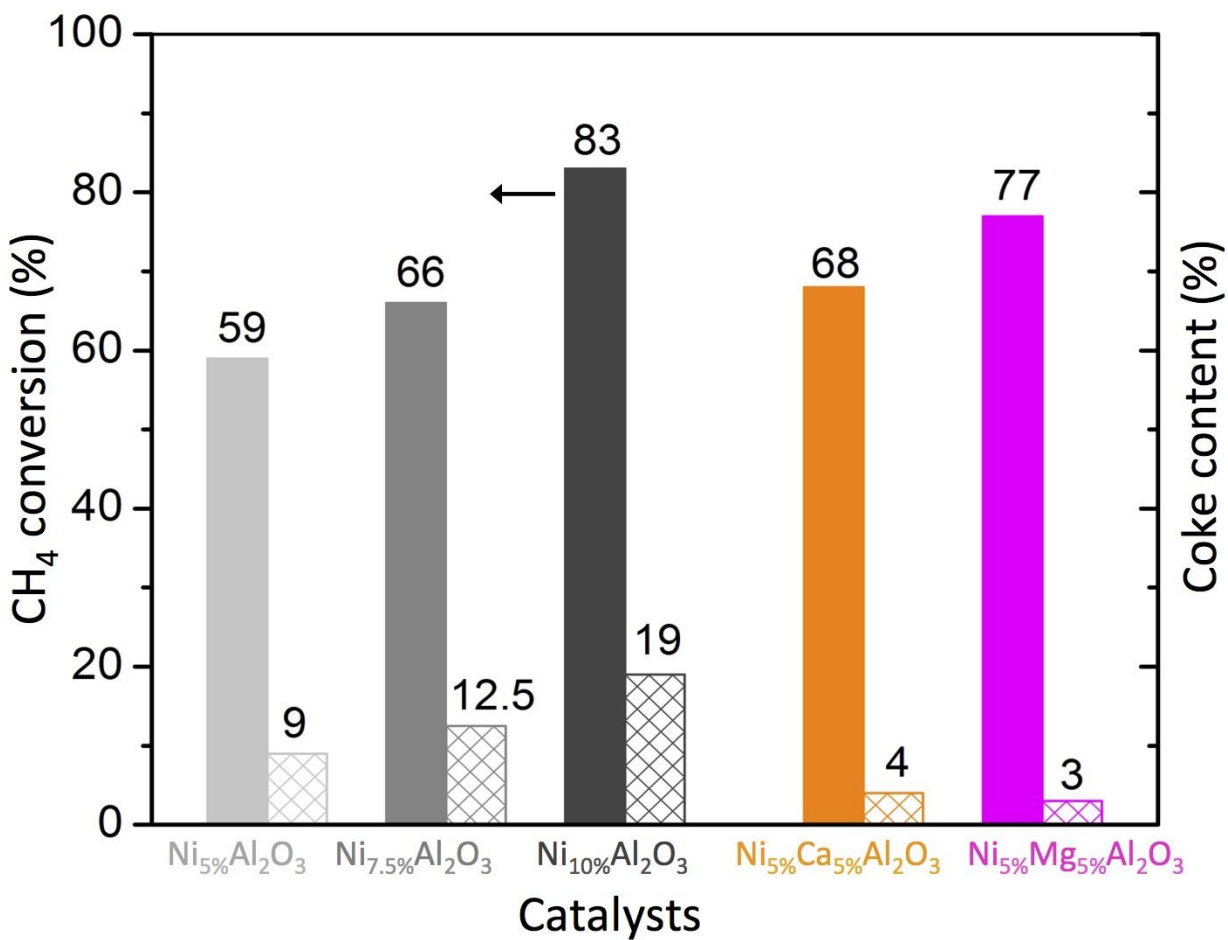
Figure 8. Raman spectra of spent (800°C/40h, $CH_4/CO_2/H_2O/Ar$ = 1/0.4/0.8/12, GHSV = 138 L.g_{cat}^{-1}.h^{-1}) catalysts: (a) $Ni_{7.5\%}Al_2O_3$ and (b) $Ni_{10\%}Al_2O_3$.
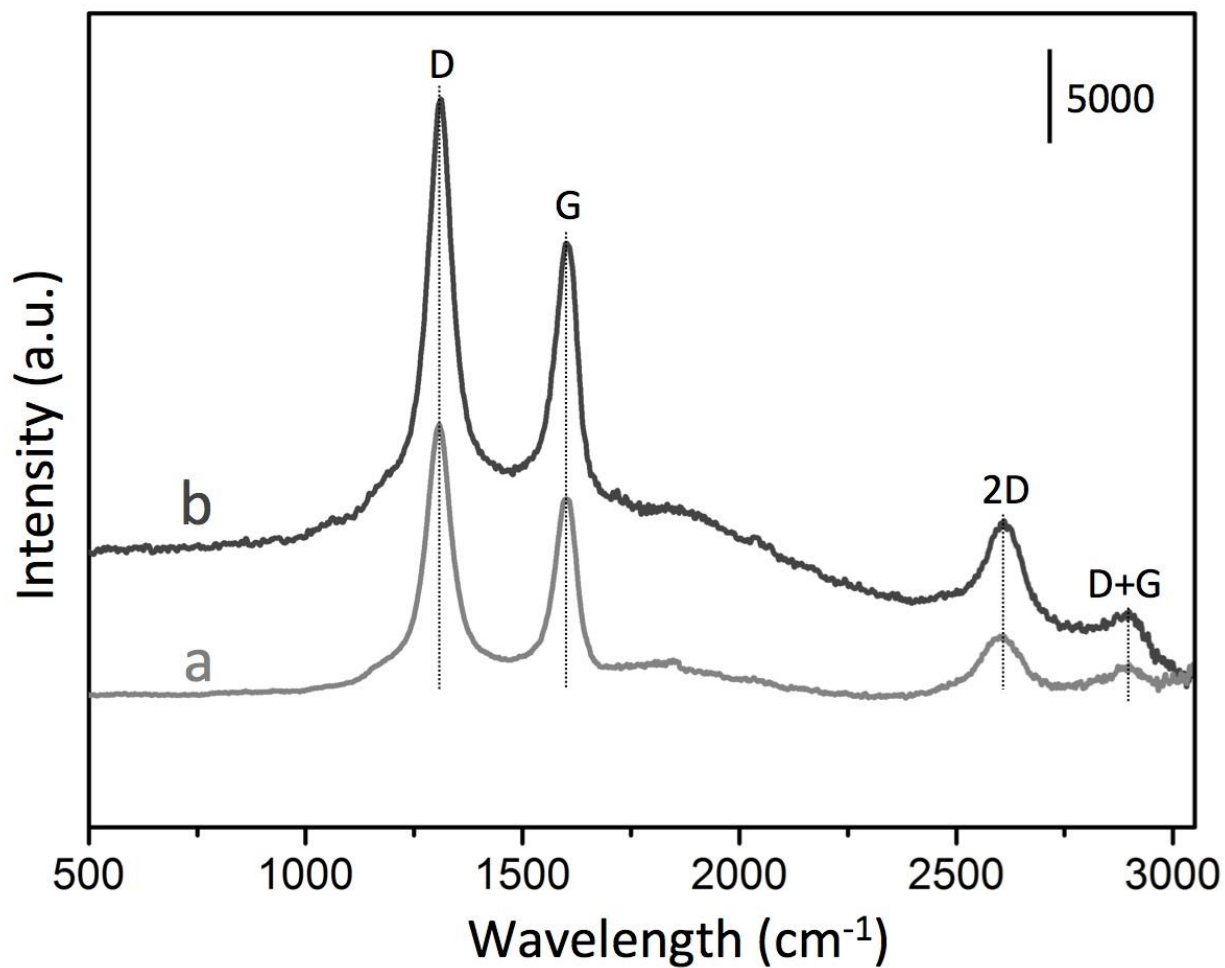
Figure 9. (A,B) SEM and (C,D) TEM micrographs of spent (800°C/40h, $CH_4/CO_2/H_2O/Ar$ = 1/0.4/0.8/12, GHSV = 138 $L.g_{cat}^{-1}.h^{-1}$) $Ni_{10\%}Al_2O_3$. Some carbon deposits are marked with arrows.
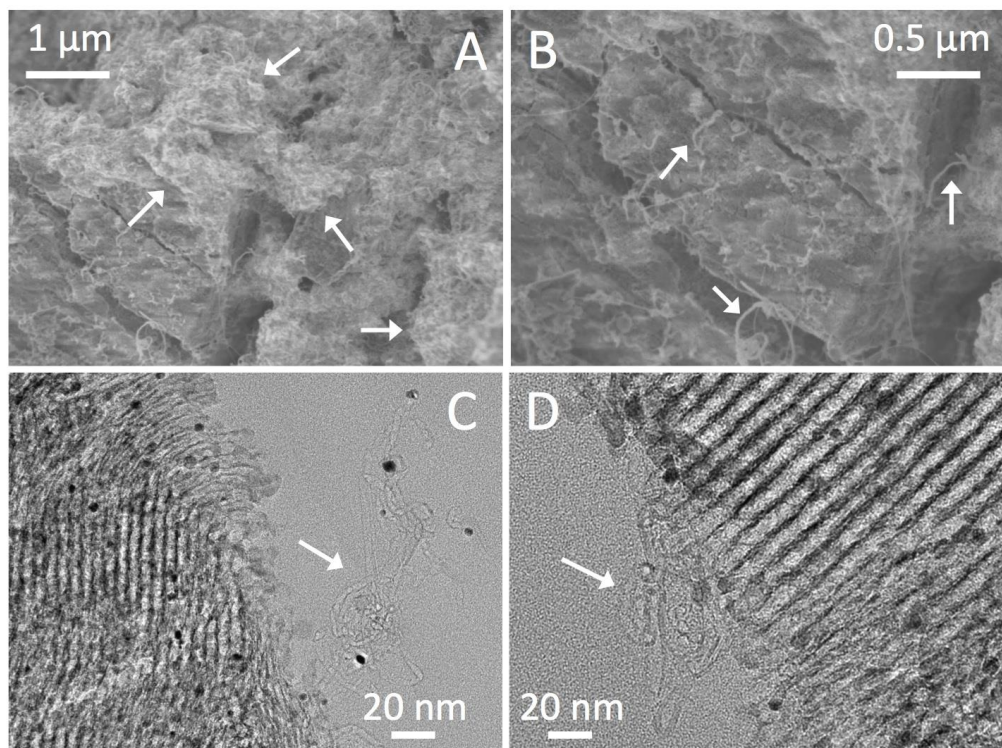
Figure 10. TEM micrographs of spent (800°C/40h, $CH_4/CO_2/H_2O/Ar$ = 1/0.4/0.8/12, GHSV =138 $L.g_{cat}^{-1}.h^{-1}$) (A-C) $Ni_{10\%}Al_2O_3$, (A'-C') $Ni_{5\%}Ca_{5\%}Al_2O_3$ catalysts. Insets in Figures A, C and B' (dashed-lines) show zooms made on the specified grain zones.
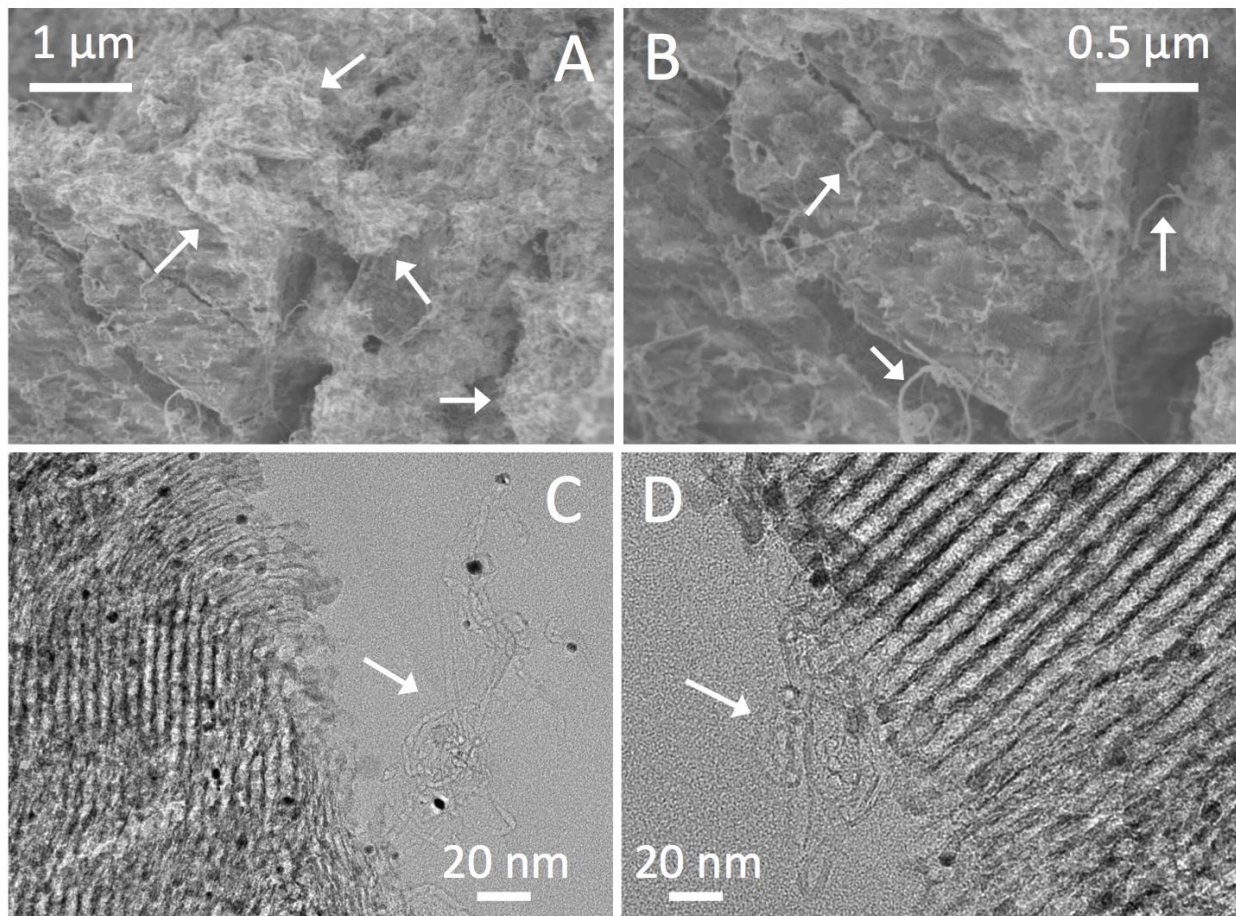
Figure 11. N_2-sorption adsorption-desorption isotherms and pore size distributions (inset) of (a) calcined, (b) reduced (800°C/3h) and (c) spent (800°C/40h, $CH_4/CO_2/H_2O/Ar = 1/0.4/0.8/12$, GHSV = 138 $L.g_{cat}^{-1}.h^{-1}$) $Ni_{10\%}Al_2O_3$. Curve (c) was obtained after re-calcination (450°C/5h in air) of the spent catalyst.
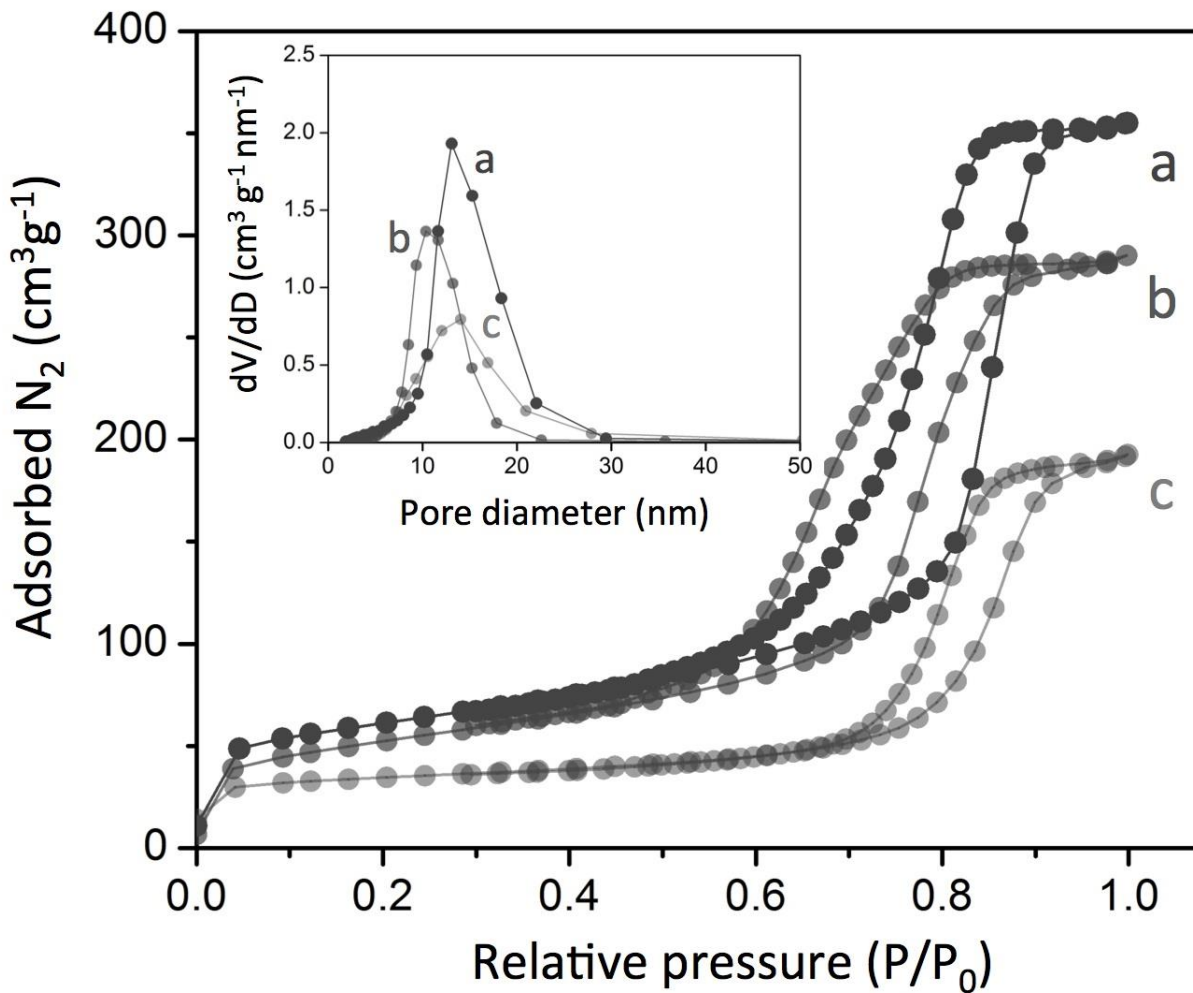
Figure 12. (A) Low and (B) wide angles XRD patterns of (a-f) reduced (800°C/3h) and (b'-f') spent (800°C/40h, $CH_4/CO_2/H_2O/Ar$ = 1/0.4/0.8/12, GHSV = 138 $L.g_{cat}^{-1}.h^{-1}$) catalysts: (a) Al_2O_3, (b,b') $Ni_{5\%}Al_2O_3$, (c,c') $Ni_{7.5\%}Al_2O_3$, (d,d') $Ni_{10\%}Al_2O_3$, (e,e') $Ni_{5\%}Ca_{5\%}Al_2O_3$ and (f,f') $Ni_{5\%}Mg_{5\%}Al_2O_3$. An offset was applied along the *Y*-axis for the sake of clarity.
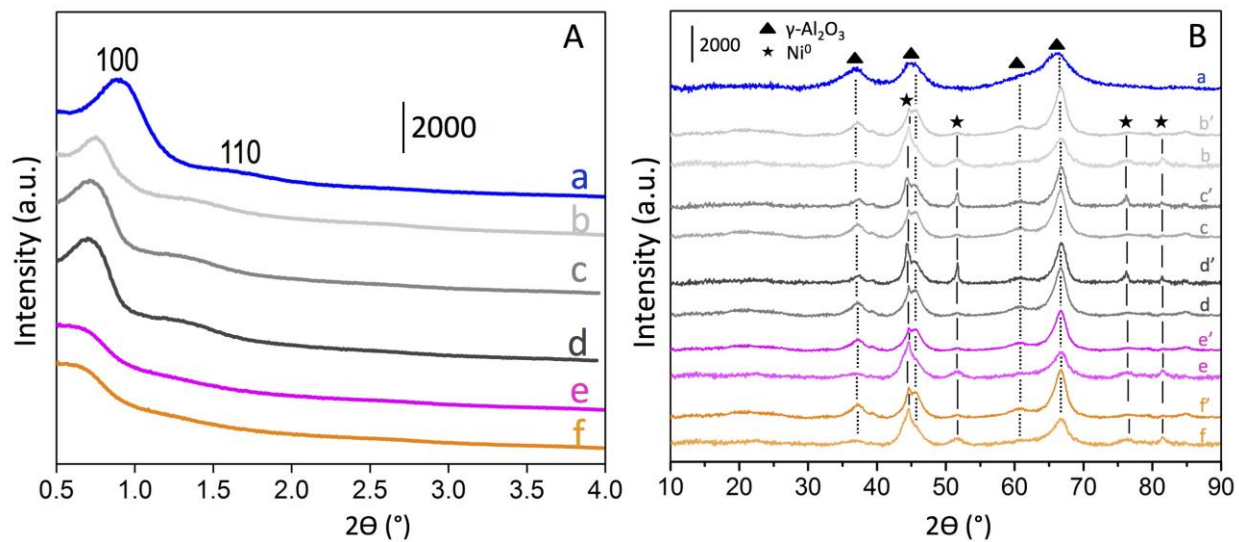
Figure 13: Schematic representation of the spent catalysts. The CSDRM reaction takes place on the dispersed Ni^0 active nanoparticles remaining occluded (stabilized) in the preserved alumina-based mesoporous network. Adsorbed activated C* and O* species (formed upon dissociative adsorption of CH_4, CO_2 and H_2O, Table 7) are also represented. The more numerous O* on more basic catalysts (right hand side) react with neighbour adsorbed C* leading to oxidative carbon removal ($R_I \approx R_{II}$ and R_{III}). On the contrary, rapid carbon polymerization takes place on less basic catalysts (($R_I >$ R_{II} and R_{III}, left hand side) resulting in the growth of carbon nanotubes on external Ni^0 nanoparticles that simultaneously suffer sintering.